JGR Solid Earth

RESEARCH ARTICLE
10.1029/2023JB028460

# Remagnetization of Pre-Fan Sediments Offshore Sumatra: Alteration Associated With Seismogenic Diagenetic Strengthening

**Tao Yang[1,2], Katerina E. Petronotis[3], Gary D. Acton[3], Xixi Zhao[4,5], Farid Chemale Jr.[6], and Paulo M. Vasconcelos[7]**

[1]Key Laboratory of Intraplate Volcanoes and Earthquakes (China University of Geosciences, Beijing), Ministry of Education, Beijing, China, [2]State Key Laboratory of Geological Processes and Mineral Resources, School of Geophysics and Information Technology, China University of Geosciences, Beijing, China, [3]International Ocean Discovery Program, Texas A&M University, College Station, TX, USA, [4]Department of Ocean Science and Engineering, Southern University of Science and Technology, Shenzhen, China, [5]Department of Earth and Planetary Sciences, University of California, Santa Cruz, CA, USA, [6]Programa de Pós-Graduação em Geologia, Universidade do Vale do Rio dos Sinos, São Leopoldo, Brazil, [7]UQ-Ages Laboratory, School of Earth and Environmental Sciences, The University of Queensland, Brisbane, QLD, Australia

**Abstract** Increases in temperature and pressure caused by rapid burial of sediments seaward of the Sumatra subduction zone have been hypothesized to trigger dehydration reactions that diagenetically strengthen sediments and contribute to the formation of an over-pressured pre-décollement, which together facilitate the occurrence of large shallow earthquakes. We present paleomagnetic, rock magnetic, and electron microscopic analyses from drill cores collected offshore Sumatra at Site U1480 during IODP Expedition 362 that support this hypothesis. The older pre-fan units (Late Cretaceous to early Paleocene) were deposited when Site U1480 was moving rapidly northward with the Indian plate from a paleolatitude of 50° to 30°S, which would equate to expected absolute paleomagnetic inclinations of 70°–43°. Most of the older pre-fan sediments, however, have shallow observed inclinations (shallower than ±20°), indicating that the sediments were overprinted when Site U1480 was located near the paleoequator, as it has been since the early Oligocene. Electron microscopic observations reveal that the pre-existing detrital magnetite grains have undergone pervasive dissolution and alteration by hydrothermal fluids. The diagenesis observed is consistent with mineral dehydration, possibly driven by rapid burial of pelagic sediments by the ∼1250 m thick Nicobar Fan sequence. In addition, the elevated burial temperature also facilitated the smectite to illite conversion reaction. We hypothesize that chemical reactions resulted in the formation of fine-grained magnetite that records a chemical remanent magnetization overprint. This overprint is consistent with the alteration occurring after burial by the thick Nicobar Fan sequence sometime in the past few million years.

**Plain Language Summary** Sediments and rocks commonly contain magnetic minerals that record the direction and intensity of Earth's magnetic field as they are being emplaced, thus preserving an ancient record of the geomagnetic field. Subsequent alteration of the magnetic minerals caused by heating and/or fluid circulation can result in the acquisition of secondary magnetizations (i.e., remagnetization) that may overprint or completely reset the primary ancient magnetization. Such remagnetization provides evidence of the physical and chemical changes that have occurred. Here through paleomagnetic, rock magnetic, and microscopic analyses of the deeper older (pre-fan) stratigraphic sequence cored offshore Sumatra, we find that hydrothermal fluids, resulting from mineral dehydration driven by rapid burial of this sequence by younger, thick Nicobar Fan sediments, led to pervasive secondary remagnetization. Consequently, the newly formed magnetite recorded a much younger paleomagnetic field, leaving a shallow overprint that probably occurred sometime in the past few million years. The dehydration reactions also increased the strength of the sediments entering the subduction zone and aided in the formation of slip surfaces (called décollements), possibly contributing to the shallow, large earthquakes that have generated tsunamis off Sumatra.

**Key Points:**

- The 60–67 Ma pre-fan sediments offshore Sumatra were most likely remagnetized since deposition of the Nicobar Fan sediments, which began at ∼9 Ma
- Remagnetization of pre-fan sediments caused by mineral dehydration may be linked to shallow seismogenic slip off Sumatra
- Magnetic properties of input sediments in the subduction margin record conditions that may have facilitated the generation of earthquakes

**Supporting Information:**

Supporting Information may be found in the online version of this article.

**Correspondence to:**

T. Yang and K. E. Petronotis,
tyang@cugb.edu.cn;
petronotis@iodp.tamu.edu

**Citation:**

Yang, T., Petronotis, K. E., Acton, G. D., Zhao, X., Chemale, F., Jr., & Vasconcelos, P. M. (2024). Remagnetization of pre-fan sediments offshore Sumatra: Alteration associated with seismogenic diagenetic strengthening. *Journal of Geophysical Research: Solid Earth*, *129*, e2023JB028460. https://doi.org/10.1029/2023JB028460

Received 4 DEC 2023
Accepted 15 AUG 2024

**Author Contributions:**

**Conceptualization:** Tao Yang, Katerina E. Petronotis, Gary D. Acton, Xixi Zhao
**Data curation:** Tao Yang, Katerina E. Petronotis, Gary D. Acton, Xixi Zhao, Farid Chemale Jr., Paulo M. Vasconcelos
**Funding acquisition:** Tao Yang, Katerina E. Petronotis, Gary D. Acton, Xixi Zhao
**Investigation:** Tao Yang, Katerina E. Petronotis, Gary D. Acton, Farid Chemale Jr., Paulo M. Vasconcelos



## 1. Introduction

The Sumatra-Andaman subduction margin is characterized by an atypically thick and wide trench wedge originating from the subduction of exceptionally thick sedimentary sequences that reside on top of the Indian plate as

**Methodology:** Tao Yang, Katerina E. Petronotis, Gary D. Acton, Xixi Zhao, Farid Chemale Jr., Paulo M. Vasconcelos
**Resources:** Tao Yang, Katerina E. Petronotis, Gary D. Acton, Xixi Zhao
**Validation:** Tao Yang, Katerina E. Petronotis, Gary D. Acton, Xixi Zhao
**Writing – original draft:** Tao Yang, Katerina E. Petronotis, Gary D. Acton, Xixi Zhao
**Writing – review & editing:** Tao Yang, Katerina E. Petronotis, Gary D. Acton, Xixi Zhao, Farid Chemale Jr., Paulo M. Vasconcelos

it begins to sink beneath the Burma plate (McNeill et al., 2017). The thickness of the incoming sediment sequence and the resulting size of the trench wedge are believed to be important factors in controlling the location and generation of large, tsunamigenic earthquakes (Geersen et al., 2013; Hüpers et al., 2017).

Specifically, Geersen et al. (2013) hypothesized that the high deposition rates associated with the Nicobar Fan results in extreme thickening of the sedimentary section on the Indian plate prior to it reaching the trench (Figure 1). This thickening causes mechanical compaction, increases temperature, and liberates fluids in the deeper sediments. This has two consequences: (a) it facilitates the formation of an over-pressured pre-décollement (i.e., a proto-décollement surface seaward of the forearc), which would preferably nucleate within a deep sedimentary interval with relatively high porosity, and (b) it strengthens sediments through diagenetic reactions that increase lithification. Evidence of pre-décollement formation comes from seismic reflection profiles across the Sumatra-Andaman margin, which contain a high amplitude negative polarity (HANP) seismic reflector near the base of the sedimentary section (Dean et al., 2010) (Figure 1b). The formation of the décollement and the strengthening of sediments is hypothesized to facilitate the occurrence of large, shallow earthquakes along the western Sumatra margin. Furthermore, the sediment strengthening explains why the earthquakes along this margin occur closer to the seaward limits of the forearc than at other subduction zones where only thin sedimentary sections are being subducted. For example, the 2004 Mw 9.2 Sumatra earthquake occurred some 160 km offshore along a 1,300-km-long rupture that runs just east of the seaward limit of forearc from northern Sumatra to the Andaman Islands (Ammon et al., 2005; Lay et al., 2005) (Figure 1a).

The focus of International Ocean Discovery Program (IODP) Expedition 362 (Sumatra Subduction Margin) was to characterize the lithologic, physical, chemical, and thermal properties of sediments and rocks entering the Sumatra subduction zone to understand the evolution of that margin and the origin of the large Sumatra earthquakes (McNeill et al., 2016). During the expedition, Sites U1480 and U1481 were cored in the Wharton Basin to depths of 1,432 m below seafloor (mbsf) in Hole U1480G and 1500 mbsf in Hole U1481A (McNeill et al., 2017) (Figure 1).

Onboard geochemical analyses showed an ∼80-m thick pore fluid freshening anomaly marked by sharp decrease in chloride between 1250 and 1330 mbsf at Site U1480 (McNeill et al., 2017). Thermal modeling done by Hüpers et al. (2017) suggested that the freshening of the pore fluid was caused by silica dehydration reactions that occurred <9 Ma, and possibly as recently as 0.1 Ma, following rapid burial of the deep hemipelagic to pelagic sediments by the Nicobar Fan sediments. This depth also corresponds with the HANP seismic horizon associated with the pre-décollement (Figure 1b; Dean et al., 2010; McNeill et al., 2017). These observations are consistent with the hypothesis proposed by Geersen et al. (2013), which we will refer to as the "diagenetically induced sediment strengthening and décollement inception" (DISSDI) hypothesis.

In this study, rock magnetic and paleomagnetic analyses were carried out mainly on pre-fan sedimentary and igneous rocks from the bottom ∼180 m of Hole U1480G, most of which are Late Cretaceous to Paleocene in age. Our study originally aimed to provide magnetostratigraphic age constraints and new paleolatitudinal estimates for the Indian plate. These types of studies require that the rocks retain the original natural remanent magnetization (NRM) that they acquired when they were deposited or emplaced. Given that the Indian apparent polar wander path (APWP) was already relatively well constrained over the past 70 Ma (Acton, 1999; Torsvik et al., 2012), the expectation was that rocks of Late Cretaceous to Paleocene age at Site U1480 would have moderate to steep (43°–70°) paleomagnetic inclinations. While some of the lithologic units did have steep characteristic remanent magnetization (ChRM), others showed evidence of being partly or fully remagnetized by a shallow (<20°) ambient geomagnetic field, which would indicate overprinting occurred sometime from about Miocene to recent time. This overprint is consistent with these lithologic units being thermally and/or chemically altered by processes in accord with the DISSDI hypothesis. Given the relevance of this hypothesis in understanding devasting earthquakes, the emphasis of our study changed to documenting the stratigraphic extent of the overprint, estimating its timing, and investigating how diagenesis has affected the magnetic mineralogy.

## 2. Materials and Methods

### 2.1. Geologic Setting and Samples

Drill Sites U1480 and U1481 of IODP Expedition 362 are located on the Indian plate, east of the Ninetyeast Ridge and ∼250 km southwest of the Sumatra-Andaman subduction zone (Figures 1a and 1b). At Site U1480, situated at

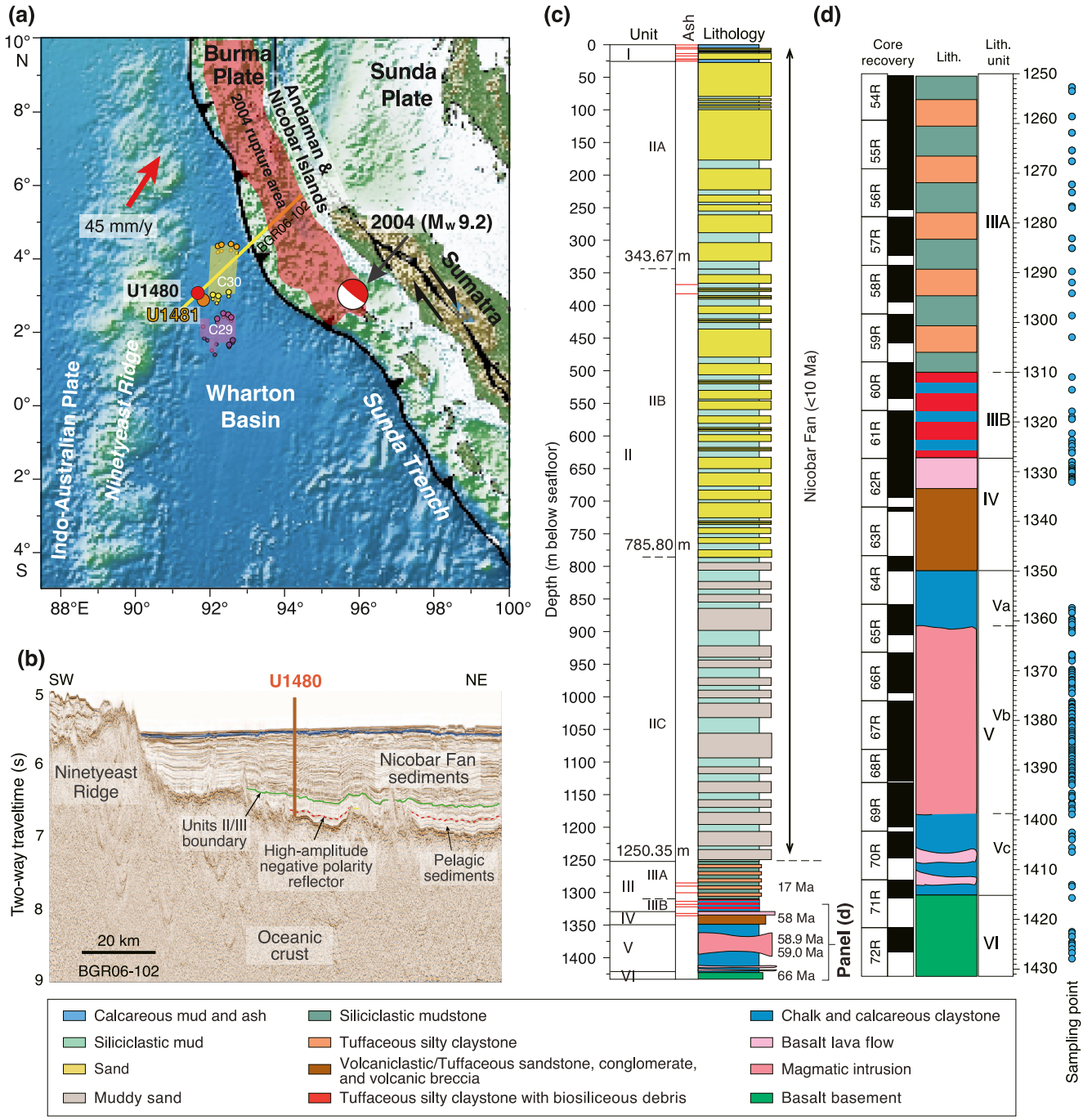


**Figure 1.** (a) Map of the north Sumatran subduction zone showing the location of drill Sites U1480 (red dot) and U1481 (orange dot) of International Ocean Discovery Program (IODP) Expedition 362 in the Wharton Basin, and the epicenter of the 2004 Mw 9.2 Sumatra–Andaman earthquake. Rupture location of the earthquake is from Briggs et al. (2006). Marine magnetic anomaly picks from Jacob et al. (2014) are shown with dots (orange and yellow dots correspond to the old and young ends of Chron C30n; pink and purple dots correspond to the old and young ends of Chron C29n). Red arrow with number is a convergence vector (mm/year). (b) Interpreted seismic profile BGR06-102 (yellow line in panel a) showing North Sumatran subduction input (i.e., Nicobar Fan and pelagic sediments), with Site U1480 (modified from McNeill et al., 2017). (c) Stratigraphic section showing lithostratigraphic (sub)units for Site U1480 (modified from McNeill et al., 2017), mbsf = meters below sea floor. Sediment ages are from Backman et al. (2019). (d) A close-up view of the studied interval (i.e., Units III-VI) with core recovery. The dark parts indicate core recovered, with adjacent numbers indicating core numbers (R indicates the rotary core barrel type). Blue dots mark the sampling points.

a water depth of 4,148 m in the Wharton Basin, Holes U1480E–U1480G recovered a 1431.63 m sequence of sediments and rocks (Figure 1c). This sequence is composed of (a) ~1,250 m of Nicobar Fan siliciclastic sediments (Units I–II); (b) ~165 m of pelagic sediments, volcaniclastic and tuffaceous sandstones, basalts, and

diorites (Units III–V); and (c) 16 m of ocean crust basalts (Unit VI) (McNeill et al., 2017; Figure 1c). A detailed description of the preliminary lithologic, physical properties, and geochemical measurements on the succession of sampled sediments/rocks is provided in the IODP Site U1480 and Site U1481 chapters (McNeill et al., 2017).

Our study focuses on the deeper, pre-Nicobar Fan interval of Hole U1480G (Figure 1d), which includes the following units:

1. Unit VI (1415.35–1431.63 mbsf) comprises Late Cretaceous upper ocean crust basalts (Backman et al., 2019; McNeill et al., 2017). Based on a study of marine magnetic anomalies in the Wharton Basin (Jacob et al., 2014), Site U1480 is located near the C29r/C30n marine magnetic anomaly boundary (Figure 1a), suggesting the basalts are ∼67 million years old (Backman et al., 2019).
2. Unit V (1349.80–1415.35 mbsf) comprises Late Cretaceous chalk and calcareous claystone with late Paleocene magmatic intrusions (Figure 1d; Backman et al., 2019; McNeill et al., 2017). The unit can be divided into an upper sedimentary package (referred to here as "Subunit Va"), a middle ∼37-m thick diorite intrusion body ("Subunit Vb"; 1361.24–1398.69 mbsf), and an underlying sedimentary package ("Subunit Vc") (Figure 1d). Two fresh samples were collected from the Subunit Vb diorite intrusion from 1392.6 to 1394.1 mbsf for $^{40}Ar/^{39}Ar$ dating. Both samples were dated in duplicate by laser incremental-heating analysis. The $^{36}Ar/^{40}Ar$ versus $^{39}Ar/^{40}Ar$ correlation diagrams for the two samples yield isochron ages of 58.87 ± 0.19 Ma and 59.02 ± 0.18 Ma (see Text S1 in Supporting Information S1 for details of the analytical procedures; Kuiper et al., 2008; Renne et al., 2009; Steiger & Jäger, 1977; Vasconcelos et al., 2002). An isochron for the pooled results for all four grains indicates that the age of intrusion and cooling of the diorite is 58.93 ± 0.15 Ma (MSWD = 1.1, $n$ = 41; $^{40}Ar/^{36}Ar$ intercept = 304.3 ± 3.6).
3. Unit IV (1327.18–1349.80 mbsf) comprises Late Cretaceous to late Paleocene tuffaceous sandstone, which is overlain by basalt flows separated by a volcaniclastic breccia (Backman et al., 2019; McNeill et al., 2017; Figure 1d).
4. Unit III (1250.35–1327.18 mbsf) comprises late Paleocene to late Miocene tuffaceous silty claystone with chalk and minor biosiliceous debris (McNeill et al., 2017). The most notable difference is that Subunit IIIA (1250.35–1310.10 mbsf) is gray-green colored with some brown intervals and Subunit IIIB (1310.10–1327.18 mbsf) is mostly reddish brown. There is an ∼41 m.y. hiatus that occurs near the bottom of lithologic Subunit IIIB, which Backman et al. (2019) place in Section 362-U1480G-61R-7W. The hiatus occurs below two Miocene age samples [362-U1480G-61R-5W, 20 cm (1323.55 mbsf) dated at 17.02 Ma and 362-U1480G-61R-6W, 113–115 cm (1325.96 mbsf) dated only as early Miocene] and above a Paleocene age sample [61R-7W, 56 cm (1326.83 mbsf) dated at 58.1 Ma]. Over the past 10 Ma, Unit III has been overlain by 1250 m of Nicobar Fan siliciclastic sediments, which was deposited at an average rate of between 100 and 220 m/Ma.

During IODP Expedition 362, 174 discrete samples were collected from the Hole U1480G pre-fan hemipelagic to pelagic succession and basaltic basement (Cores 362-U1480G-54R to −72R, ∼1251–1428 mbsf) for rock magnetic and paleomagnetic analyses. Samples were taken from soft sediments using "Japanese" Natsuhara-Giken plastic cubes (7 $cm^3$) and from sedimentary rocks and basalts using a double-bladed rock saw or a drill press with a 2.5-cm mini-core bit to get cubes (8 $cm^3$) or 2.5-cm diameter by 2 cm long mini-cores (10 $cm^3$), respectively. The sampling levels are indicated in Figure 1d.

### 2.2. Rock Magnetic Methods

Magnetic susceptibility (expressed on a mass-specific basis) was measured for all samples at low frequency of 976 Hz ($\chi_{976\ Hz}$) and high frequency of 15,616 Hz ($\chi_{15616\ Hz}$), respectively, in an applied field of 200 A/m with an MFK1-FA Kappabridge susceptibility meter (AGICO, Czech Republic) at the Paleomagnetic Laboratory of the State Key Laboratory of Marine Geology (PL-SKLMG), Tongji University (Shanghai, China). The low-frequency measurement (i.e., $\chi_{976\ Hz}$) represents the mass-specific low-field magnetic susceptibility ($\chi$) reported herein. Frequency-dependent magnetic susceptibility ($\chi_{fd}$%) was calculated as $\chi_{fd}\% = [(\chi_{976\ Hz} - \chi_{15616\ Hz})/\chi_{976\ Hz}] \times 100$.

Magnetic hysteresis measurements were carried out using a MicroMag™ Model 3900 vibrating sample magnetometer (VSM, Princeton Measurements Corp., USA) with a maximum applied field of 1.0 T, at the Institute of Geophysics, China Earthquake Administration (IGP-CEA, Beijing, China). The hysteresis parameters such as saturation magnetization ($M_s$), saturation remanence ($M_{rs}$), and coercive force ($B_c$) were determined from the hysteresis loops, while the remanence coercive force ($B_{cr}$) was determined through progressive back-field

demagnetization of the isothermal remanent magnetization imparted at 1 T. First-Order Reversal Curves (FORCs; Roberts et al., 2000) measurements for selected samples were conducted using the VSM 3900 to examine magnetostatic interactions and characterize the magnetic domain state. For each FORC diagram, a total of 120 curves were measured with an averaging time of 0.1–0.2 s per data point and a field increment of approximately 2 mT. FORC distributions were produced using the FORCinel package (Harrison & Feinberg, 2008) and FORCtool software (https://forctool.com, Surovitskii et al., 2022), with the conventional FORC processing methods (Pike et al., 1999).

Thermomagnetic analysis was conducted on at least 2 samples from each subunit and a total of 20 samples, using a MFK1-FA Kappabridge coupled with a CS-4 high-temperature furnace at the IGP-CEA. The analysis was carried out at a field of 200 A/m and a frequency of 976 Hz. The samples underwent heating to 700°C in an argon atmosphere at a rate of ∼11°C/min, followed by cooling to room temperature.

Low-temperature magnetic measurements down to 5 K were carried out using a Quantum Design Magnetic Property Measurement System (MPMS, Quantum Design Inc., USA) either at the Institute of Geomechanics, Chinese Academy of Geological Sciences (Beijing, China) with the model MPMS 3 or at the State Key Laboratory for Artificial Microstructure and Mesoscopic Physics, Peking University (Beijing, China) with the model MPMS XL-7. Low-temperature demagnetization of saturation isothermal remanent magnetization imparted in a 2.5 T field at 5 K (LT-SIRM) was measured twice. Initially, the LT-SIRM was measured after cooling the sample from room temperature (300 K) to 5 K in zero field (termed ZFC), and subsequently after cooling the sample from 300 to 5 K in a 2.5 T field (termed FC). Also, a SIRM was imparted at 300 K in a 2.5 T field (RT-SIRM) and measured as a function of temperature during a 300 K–5 K–300 K cycle in a zero magnetic field. Heating and cooling rates during these measurements were 5 and 10 K/min, respectively.

### 2.3. Paleomagnetic Methods

Samples were demagnetized at the PL-SKLMG. We used both alternating-field (AF) and thermal demagnetization (TD) techniques based on the lithology and magnetic coercivity properties of the samples. The magnetic remanence of samples was measured with a horizontal pass-through 2G liquid-helium free Mode 755-4K superconducting rock magnetometer (2G Enterprises, USA) equipped with the classic manufacturer automatic sample handling system and in-line AF coils. Successive AF demagnetization of 152 discrete samples along three perpendicular axes was performed in 2 mT steps up to a peak field of 20 mT, 5 mT steps up to a peak field of 40 mT, 10 mT steps up to a peak field of 80 mT, and finally a step at 100 mT. Thermal demagnetization was performed on 6 discrete samples using a Model TD-48SC thermal demagnetizer (ASC Scientific Company, USA) in 40°C steps from 80° to 600°C. The declination and inclination of different remanence components was calculated by principal component analysis (PCA; Kirschvink, 1980), using PuffinPlot (Lurcock & Wilson, 2012) and Zplotit (Acton, 2011) software. Because rotary cores were not oriented during Expedition 362, interpretation focuses on magnetic inclination data and, when computing means, uses the inclination-only statistical method of Arason and Levi (2010) to calculate averages and 95% confidence limits. In addition, results of 16 samples (12 for AF, and 4 for TD) measured on the *JOIDES Resolution* in 2016 (McNeill et al., 2017) were re-processed and are included in this study.

### 2.4. Electron Microscopic Analyses

Scanning electron microscopy/energy dispersive X-ray spectrometry (SEM/EDS) analyses were carried out on both bulk samples and thin sections. For bulk sample observations, rock slices/chips with smooth flat surfaces were coated with ∼100 nm of gold and imaged using a HITACHI S-3400N SEM (Hitachi, Japan) equipped with a Bruker X-Flash 5010 EDS detector (Bruker, Germany) at the PetroChina Research Institute of Petroleum Exploration & Development (Beijing, China). Meanwhile, a subset of representative samples was cut, mounted onto glass slides, and then grounded and polished to a thickness of ∼30 μm. For soft sediments and sedimentary rocks, samples were dried in an oven at ∼40°C, impregnated with epoxy resin under vacuum, and then sectioned, ground and polished. Carbon-coated thin sections were imaged using a Zeiss Sigma SEM system (Carl Zeiss, Germany) coupled with an Oxford X-Max $50^N$ EDS detector (Oxford Instruments, UK) at the State Key Laboratory of Earthquake Dynamics, Institute of Geology, China Earthquake Administration (Beijing, China). For both observations, backscattered electron (BSE) images were obtained at a working distance of 8.5 mm and an

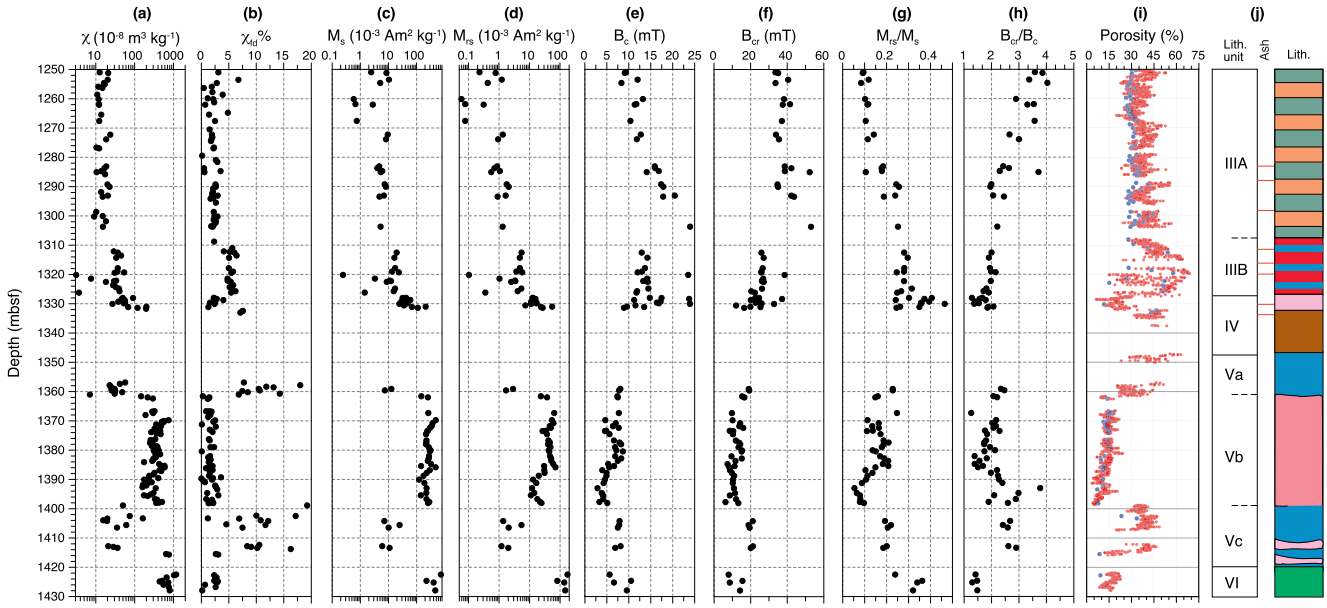


**Figure 2.** Magnetic properties of the studied sequence (lithostratigraphic Units III-VI), Hole U1480G. (left to right) Downhole (a) mass-specific low-field magnetic susceptibility ($\chi$), (b) frequency-dependent magnetic susceptibility ($\chi_{fd}$%), (c) saturation magnetization ($M_s$), (d) saturation remanence ($M_{rs}$), (e) coercive force ($B_c$), (f) remanent coercive force ($B_{cr}$), (g) ratio between $M_{rs}$ and $M_s$, (h) ratio between $B_{cr}$ and $B_{cr}$, (i) porosity, and (j) lithology. The reader is referred to Figure 1 for more details about lithology. In panel (i), porosity data from shipboard moisture and density (MAD) measurements of discrete samples are in blue (McNeill et al., 2017) and high-resolution porosity data are in red (Childress et al., 2024). The high-resolution porosities, which have been smoothed with a 5-point running average, indicate that (Sub)units IIIB, Va, and Vc have high porosities (from about 25% to 60%) and could be pathways for fluid migration, whereas the diorite and basalt units have very low porosity.

accelerating voltage of 15 kV. Elemental compositions were determined through point analyses of individual mineral grains using the attached EDS detector.

## 3. Results

### 3.1. Rock Magnetic Properties

#### 3.1.1. Magnetic Susceptibility and Hysteresis Properties

Downhole magnetic parameters are shown in Figure 2 and summarized in Table S1. Generally, magnetic parameters show strong lithology dependence. The Unit VI basalt basement has the highest $\chi$, $M_s$, and $M_{rs}$ values, followed by the Subunit Vb diorite, Unit IV basalt flows, Subunit IIIB sediments, and the sedimentary packages in Subunits Va and Vc. Subunit IIIA sediments have the lowest $\chi$, $M_s$, and $M_{rs}$ values. $B_c$ and $B_{cr}$ trends are generally opposite to those observed in $\chi$, $M_s$, and $M_{rs}$. Notably, $\chi_{fd}$% generally ranges <6% in most of the (Sub)units except for Subunits Va and Vc, where relatively high values of $\chi_{fd}$%, ranging from ~7% to 20%, are present (Figure 2b), suggesting a considerable contribution of fine-grained magnetic particles around superparamagnetic/single domain (SP/SD) boundary in these sediments (e.g., Dearing et al., 1996; Maher & Thompson, 1999). It is also noteworthy that overall hysteresis ratios $M_{rs}/M_s$ increase and $B_{cr}/B_c$ decrease with depth within Unit III (Figures 2g and 2h; Table S1).

After high-field slope correction, all samples show closed hysteresis loops that approach magnetic saturation in a field of ~300 mT (Figures 3a–3p), indicating that the magnetic minerals are dominated by low-to-intermediate coercivity ferrimagnetic mineral(s). However, most of the Unit III sediments usually are still not magnetically saturated at above 500 mT (Figures 3a–3e), suggesting the contribution of higher coercivity mineral(s). This is compatible with their wasp-waisted behavior characterized by the positive values of the hysteresis loop shape parameter $\sigma_{hys}$ (Fabian, 2003), arising from mixtures of different populations with highly contrasting coercivities (e.g., magnetite and hematite; Roberts et al., 1995). In contrast, the other samples have dominantly negative $\sigma_{hys}$ values, suggesting a potbellied behavior. This is indicative of typical mixture of SD and small SP particles (Roberts et al., 2011; Tauxe et al., 1996). On a Day-Dunlop plot (Figure 3q; Day et al., 1977; Dunlop, 2002), all

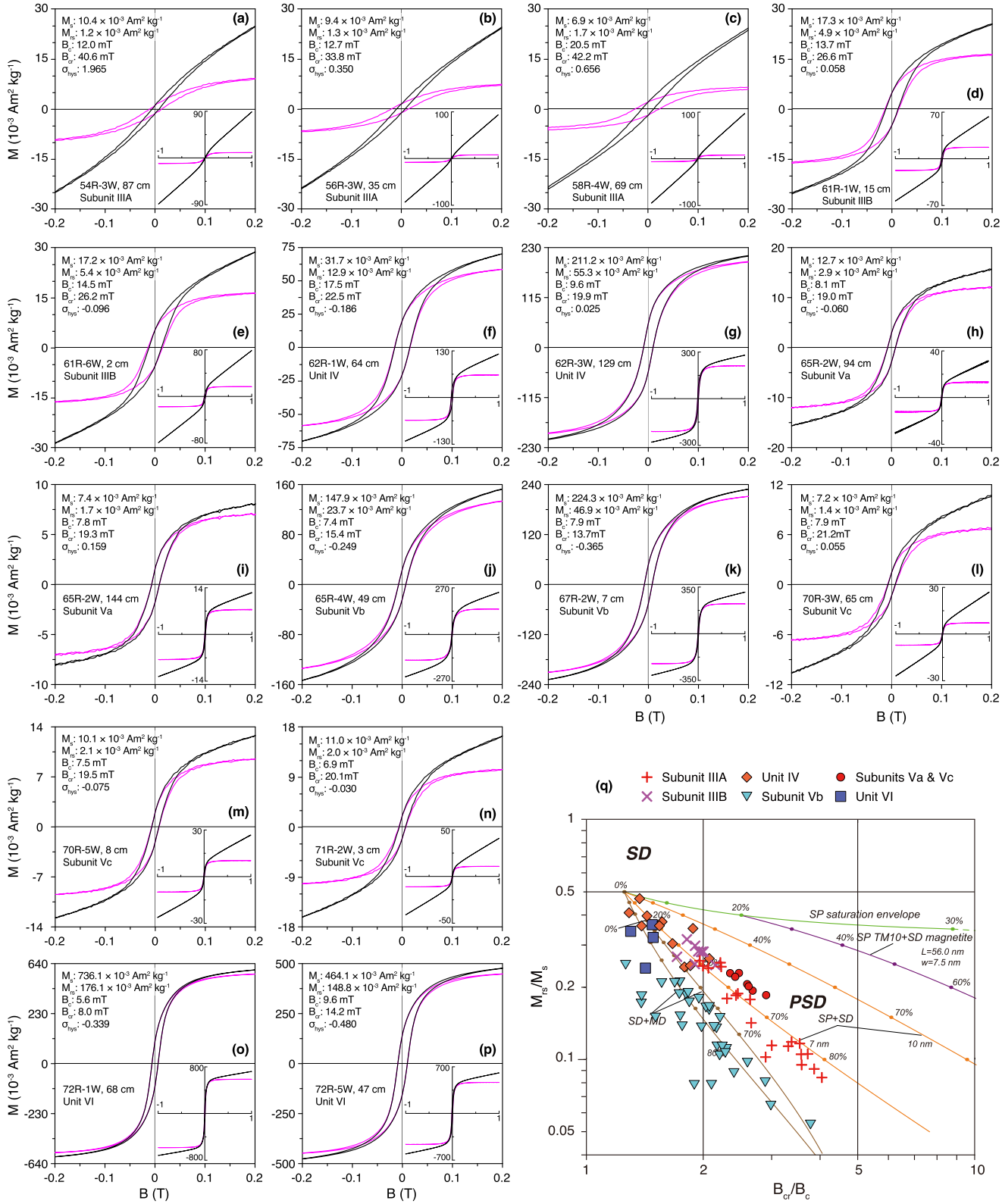


**Figure 3.**

samples are located in the pseudo-SD (PSD) range. PSD state is recently suggested to be equivalent to the "vortex state" (Roberts et al., 2017), so hereafter it is referred to as "vortex state." The Unit VI basalt basement, Subunit Vb diorite, and Unit IV basalt flow samples follow the magnetite SD + multidomain (MD) mixing curve. Most of the Subunit IIIA samples are located along the SP (7 nm) + SD mixing curves of Dunlop (2002), with the SP contribution decreasing with depth. This is also demonstrated by their hysteresis parameter variations against depth (Figures 2g and 2h). Finally, the Subunit IIIB, Va, and Vc sedimentary samples occupy a unique position on the Day-Dunlop plot: they are located between the SP (7 nm) + SD and SP (10 nm) + SD mixing curves of Dunlop (2002). In particular, the Va and Vc sedimentary samples have a higher SP contribution (Figure 3q), which is compatible with their considerably higher $\chi_{fd}$% values (Figure 2b).

FORC diagrams also highlight these differences. FORC diagrams for samples from Subunit IIIA (Figures 4a–4c) have characteristic vortex state/MD properties (Lascu et al., 2018; Muxworthy & Dunlop, 2002; Roberts et al., 2000, 2014, 2017). It is notable that FORC diagrams of samples from the upper Subunit IIIA have a relatively lower $B_c$ peak (~10 mT) (Figure 4a), whereas those from the lower Subunit IIIA have a peak at ~20–40 mT (Figure 4c). This agrees with the downhole increasing trends in $B_c$ values (Figure 2e). Similar FORC distributions with relatively small vertical spread (i.e., small interaction) are observed for Subunit IIIB sediments (Figures 4d and 4e), suggesting a mixture of non-interacting SD and vortex state/MD grains. For the majority of the basalt flow (Figures 4f and 4g), diorite (Figures 4j and 4k), and basalt basement (Figures 4n and 4o) samples, FORC diagrams exhibit closed concentric contours with a $B_c$ peak at ~10 mT and vertically dispersed distributions toward the $B_u$ axis, indicating contributions from interacting SD and vortex state particles (Lascu et al., 2018; Roberts et al., 2014). Subunit Va (Figures 4h and 4i) and Vc (Figures 4l and 4m) sedimentary samples generally show a prominent narrow $B_u = 0$ ridge for a distribution of particles with coercivities mainly disturbed between 0 and 30 mT, suggesting they contains noninteracting stable SD (SSD) particles with a substantial SP population that pull the data distribution away from SD values toward vortex state-MD-like values (Roberts et al., 2000, 2014; Rowan & Roberts, 2006). However, the expected nearly vertical contours along the $B_u$ axis in the lower quadrant that represent viscous behavior due to SP magnetite is hardly discernible here (Figures 4h, 4i, 4l, and 4m), this is probably because of limited resolution in FORC settings.

### 3.1.2. High-Temperature Dependent Magnetic Susceptibility

The representative thermomagnetic ($\chi$-T) curves are shown in Figure 5. Within Unit III, all heating runs decrease steeply to near-zero values at ~580°C (Figures 5a–5e), suggesting magnetite as a dominant magnetic carrier (Dunlop & Özdemir, 1997). The broad hump between ~320 and 500°C upon the heating run of the samples from the upper portion of Subunit IIIA (Figure 5a) may be attributed to thermal decomposition of Fe-bearing clay minerals or pyrite altering to magnetite (e.g., Hirt et al., 1993; Just & Kontny, 2012; Passier et al., 2001). Recently, relaxation of SD magnetite undergoing the SD to SP transition upon heating has been proposed as an alternative mechanism for such a thermal behavior by Zhang and Appel (2023). For samples from the middle level of Subunit IIIA, $\chi$ decreases slightly during initial heating and increases markedly at ~450°C reaching a maximum at ~550°C just before the Curie temperature of magnetite (~580°C; Figure 5b). In contrast, upon the heating runs of the samples from the lower level of Subunit IIIA, $\chi$ remains almost constant before decreasing sharply to near-zero values at ~580°C (Figure 5c). The cooling runs lie much above the heating runs, indicating heating-induced ferrimagnetic mineral neoformation. However, the elevated level of $\chi$ is decreasing from the upper to the deeper sediments. The humps in the heating runs between ~350 and 550°C are present again in Subunit IIIB sediments, with a much smaller $\chi$ elevation at the end of cooling runs (Figures 5d and 5e), compared with those in Subunit IIIA (Figures 5a–5c). It is also evident that for some samples from Unit III, a small portion of magnetic susceptibility persists above 580°C and up to 700°C (e.g., Figures 5b–5e), indicating that hematite is likely present in these samples.

**Figure 3.** (a–p) The central portion (±0.2 T) of the hysteresis loops for representative samples from lithostratigraphic Units III-VI, Hole U1480G, before (black line) and after (magenta line) high-field slope correction (using the slope above 0.7 T). Insets show the whole hysteresis loops (±1.0 T). B, applied field; M, magnetization; $M_s$, saturation magnetization; $M_{rs}$, saturation remanence; $B_c$, coercive force; $B_{cr}$, remanence coercivity; $\sigma_{hys}$, the parameter defined by Fabian (2003) to quantify the shape of hysteresis loop, positive value is indicative of "wasp-waisted" loop and negative value indicative of "potbellied" one. (q) Day-Dunlop plot (Day et al., 1977; Dunlop, 2002) for ratios of hysteresis parameters $M_{rs}/M_s$ and $B_{cr}/B_c$. Single-domain (SD), pseudo-single-domain (PSD) and multi-domain (MD) boundaries, and theoretical mixing curves for SD-MD mixes, and SD-superparamagnetic (SP) with different SP grain sizes, are shown following Dunlop (2002). Numbers adjacent to curves are volume fractions of the soft component (SP or MD) in mixtures with SD grains.

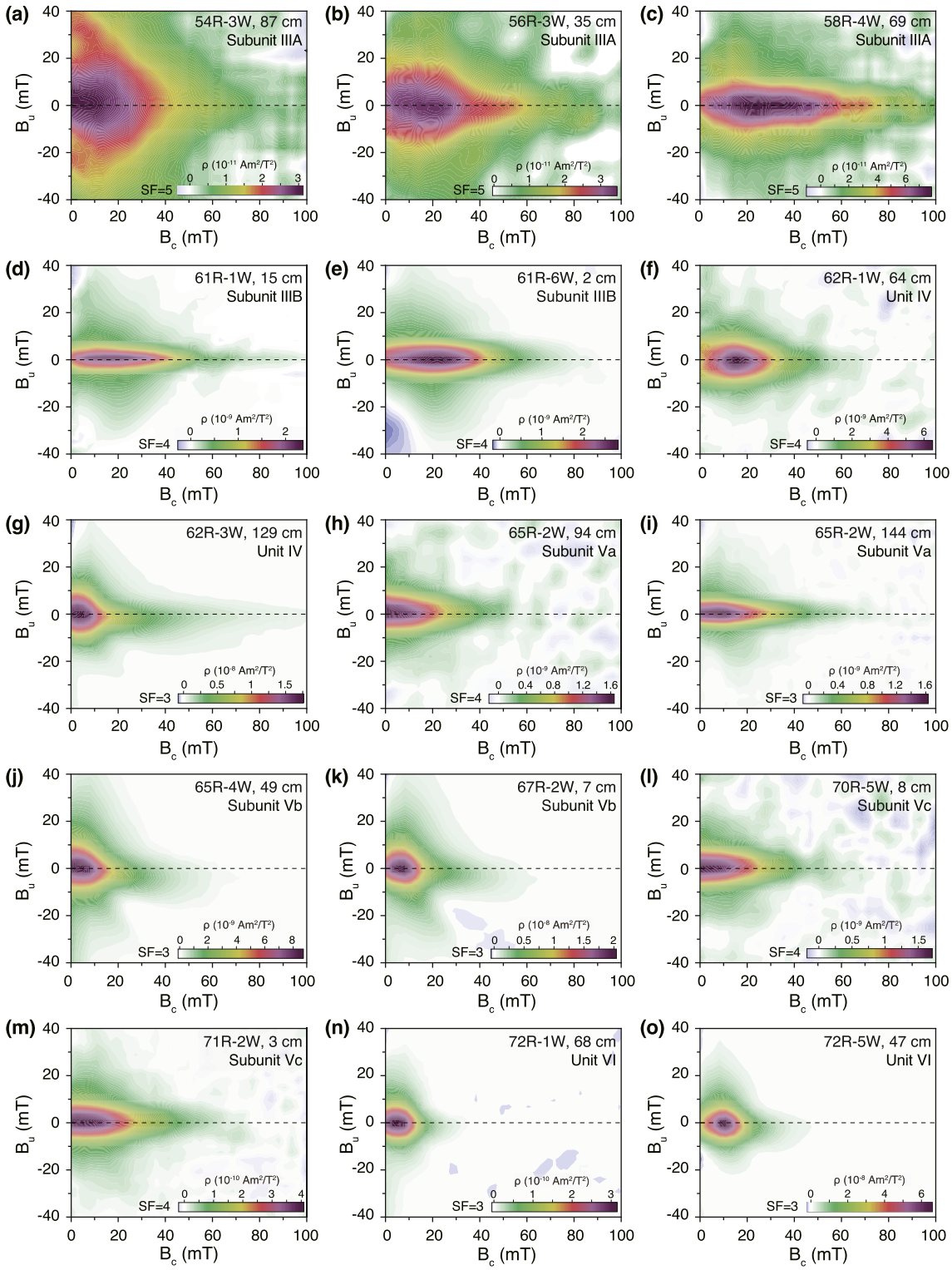


**Figure 4.** First-order reversal curve (FORC) diagrams for representative samples from lithostratigraphic Units III-VI, Hole U1480G. FORC diagrams were processed with the FORCinel package (Harrison & Feinberg, 2008) and FORCtool software (https://forctool.com, Surovitskii et al., 2022) with standard smoothing (Pike et al., 1999). SF, optimal smoothing factor; $B_c$ and $B_u$ are equivalent to a particle coercivity and a local interaction field for SD particles, respectively. Colors in each diagram represent absolute values of the FORC density (ρ).

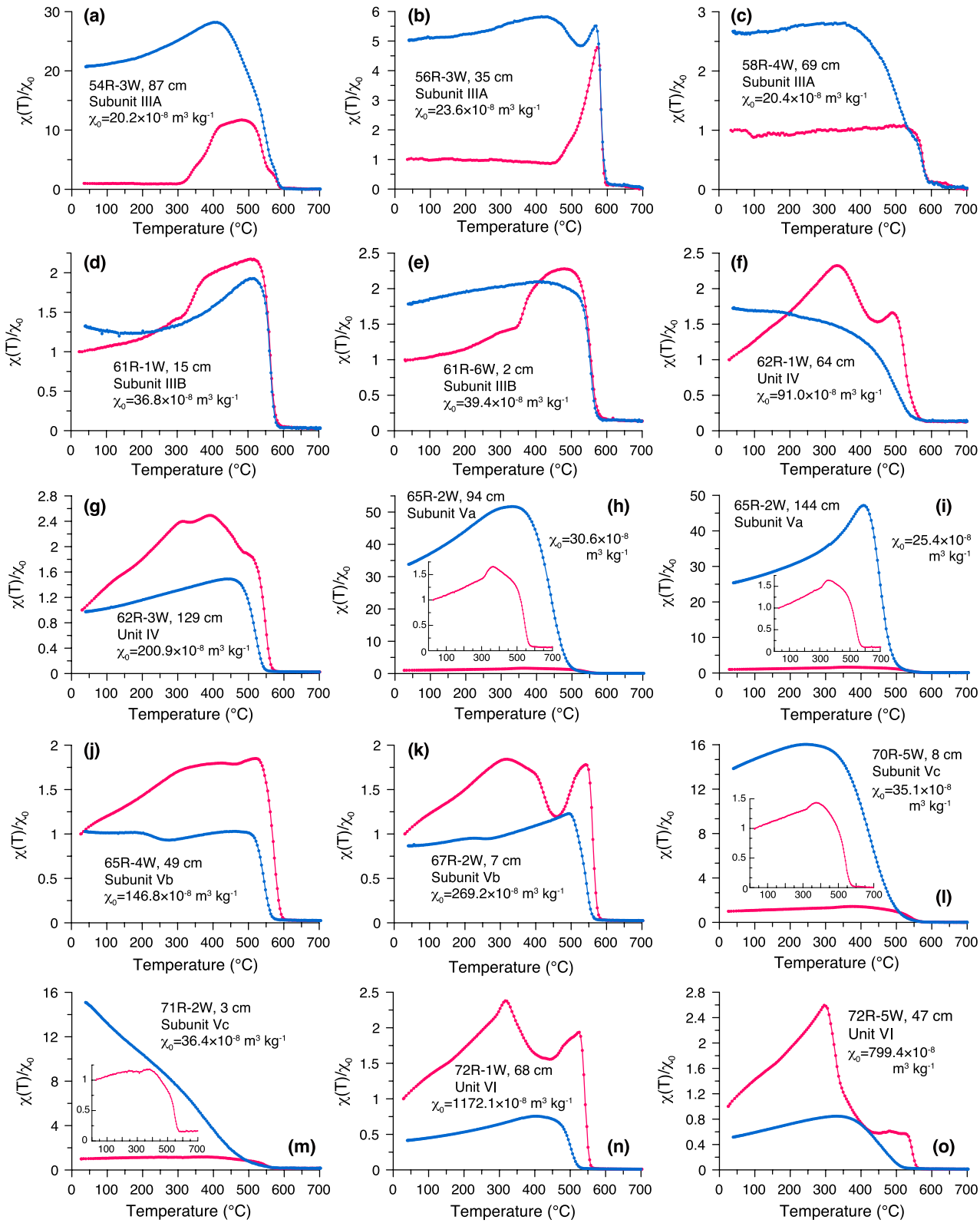


**Figure 5.** Magnetic susceptibility versus temperature (χ–T) cycles for representative samples from lithostratigraphic Units III-VI, Hole U1480G, from room temperature to 700°C in argon. Each curve is normalized by the initial magnetic susceptibility at room temperature ($\chi_0$). Red and blue lines indicate heating and cooling runs, respectively.

For Unit IV basalt flow and Subunit Vb diorite samples (Figure 5g–5k), $\chi$ increases during heating with a bump between ~150 and 450°C, although the peak is more subtle and rounded for some samples (e.g., Figures 5g and 5j). The hump is most likely caused by transition from SSD to the SP state, and the width of the hump reflects different SSD-SP transition temperatures due to a range of magnetic grain sizes (Zhang et al., 2020). The $\chi$ subsequently decreases to nearly zero at ~550–580°C, indicating (titano-)magnetite as the primary carrier (Dunlop & Özdemir, 1997). In some diorite (Figure 5k) samples, a pronounced $\chi$ peak can be observed immediately below ~550–580°C, which might represent the Hopkinson effect of (titano-)magnetite upon heating. For some Unit IV basalt flow (Figure 5f) and Unit VI basalt basement samples (Figures 5n and 5o), $\chi$ increases more rapidly with heating, and peaks at ~300–320°C. This may correspond to the presence of Ti-rich titanomagnetite (Appel & Soffel, 1985; Dunlop & Özdemir, 1997; Zhang, Appel, Basavaiah, et al., 2021), which converts to magnetite at higher temperatures associated with the followed Hopkinson peak at ~550–560°C. The cooling runs are well below the heating runs, with end $\chi$ values less than half of the initial ones. This might be caused by the destruction of Ti-rich titanomagnetite or fine-grained magnetite.

For sedimentary Subunit Va and Vc samples, $\chi$ increases with temperature with small humps present between ~350 and 500°C in the heating runs, and finally reaches near-zero values at ~580°C (insets, Figures 5h, 5i, 5l, and 5m), which indicates magnetite as the primary magnetic mineral (Dunlop & Özdemir, 1997). Upon the cooling runs, $\chi$ increases by more than an order of magnitude from the heating values, suggesting that a large amount of magnetite formed between ~600 and 700°C during the thermomagnetic treatment. This makes Subunit Va and Vc samples quite distinct from the other sedimentary samples in Unit III.

#### 3.1.3. Low-Temperature Remanence Demagnetization

Results of the low-temperature magnetic measurements display different characteristic behavior depending on the lithology of the units (Figure 6). For the sediments from Subunit IIIA, a clear Verwey transition ($T_v$) at ~120 K is present on both the ZFC/FC and RT-SIRM curves (Figures 6a and 6b). This indicates that magnetite, probably of vortex state/MD size, is present, as the remanence is not fully recovered on warming back to 300 K (e.g., Muxworthy & McClelland, 2000; Özdemir et al., 2002). For samples from the lower level of Subunits IIIA and IIIB (Figures 6c and 6d), Subunits Va and Vc (Figure 6f–6j), there is no specific low-temperature phase transition observed in ZFC/FC and RT-SIRM cooling/heating curves. This may indicate that magnetite particles in these sample are nonstoichiometric, either due to surface oxidation or cation substitution (e.g., Aragón et al., 1985; Jackson & Moskowitz, 2021; Muxworthy & McClelland, 2000; Zhang, Appel, Stanjek, et al., 2021; Özdemir & Dunlop, 2010).

A significant drop at ~30 K can be seen on the ZFC and/or FC curves of Unit VI basalt flow (Figure 6e), Subunit Vb (Figures 6g and 6h), and Unit VI basement basalts (Figures 6k and 6l). This may correspond to the dramatic transition in domain wall pinning in titanomagnetite (Church et al., 2011; Kosterov et al., 2018). RT-SIRM cycles of these samples are characterized either by a broad maximum between 300 and 250 K (Figures 6h and 6l), or by a rapid initial increase with a maximum around ~220–230 K (Figures 6g and 6k) upon cooling the RT-SIRM. Upon further cooling the RT-SIRM curves decrease rapidly, reaching minima of about 61%–93% of the initial RT-SIRM at ~15–30 K. At even lower temperatures, magnetization subsequently remains nearly constant or slightly increases. During warming back up, the RT-SIRM retraces the cooling curve between 5 and 70 K (for some Subunit Vb samples) or 5–120 K (for Unit VI samples). The warming curves then diverge from the cooling curves, and continue to increase and peak at 170–200 K. The magnetization subsequently starts to decrease and about 90% of the initial RT-SIRM is recovered at 300 K. All these observations are typical low-temperature behavior of titanomagnetite as described by Özdemir and Dunlop (2003), Kosterov (2003), and Kosterov et al. (2018), although there are some differences in their grain size as demonstrated by the above-mentioned different behavior (Kosterov et al., 2009).

### 3.2. NRM Components

Paleomagnetic results from both the shore-based and shipboard measurements are summarized in Figure 7 and Table S2 by lithostratigraphic unit. We present a detailed description of the magnetization directions starting with the basement, the oldest lithostratigraphic unit recovered in Hole U1480G, and moving upward through Unit III.

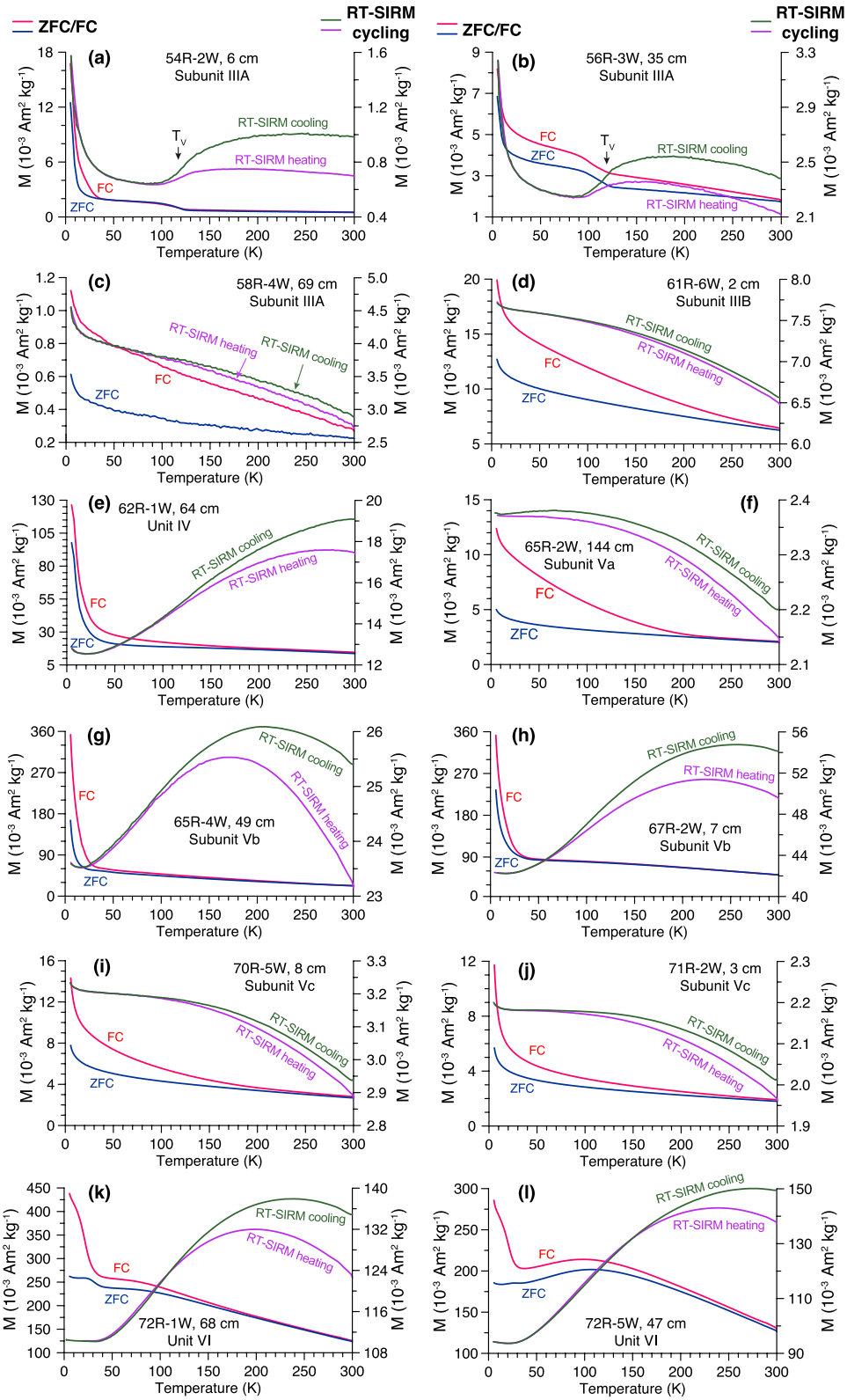


**Figure 6.** Low-temperature thermal demagnetization curves for representative samples from lithostratigraphic Units III-VI, Hole U1480G. Blue and red curves are the warming runs of a saturation isothermal remanent magnetization (SIRM) imparted to samples in a 2.5 T magnetic field after cooling the sample to 5 K in zero field (termed ZFC) and in a 2.5 T field (termed FC), respectively. Magenta and green curves are warming and cooling runs of a room temperature SIRM (RT-SIRM) imparted to samples in a 2.5 T magnetic field, respectively. Arrows with "Tv" indicate the Verwey transition of magnetite.

#### 3.2.1. Unit VI (Ocean Crust Basalts, 1415.35–1431.63 mbsf)

We analyzed 11 discrete samples from Unit VI (Figure 7). For the majority of samples, a well-resolved, high-coercivity component (HCC) can be isolated. In this case, the HCC is removed mainly between 10 and 30 mT with little to no NRM remaining above 30 mT. HCCs of the deepest 2 samples have a steep negative inclination (with an average ± std. of −55.9° ± 7.6°, Figure 7k; an example shown in Figure 8a), whereas the HCCs of 9 samples above have an intermediate positive inclination (average ± $\alpha_{95}$: 32.8° ± 8.3°, Figure 7k; an example shown in Figure 8b). A few samples have a steep, low-coercivity component (LCC) that is easily removed at demagnetization with a peak field of 10 mT (Figure 8b). Such a component is common in all drill cores and is interpreted as a drilling-induced overprint (McNeill et al., 2017; Yang et al., 2019).

#### 3.2.2. Unit V (Sedimentary Package Intruded by Diorite, 1349.80–1415.35 mbsf)

Results were obtained from 9 samples from the upper sediments (Subunit Va), 72 samples from the diorite (Subunit Vb), and 10 samples from the lower sediments (Subunit Vc) (Figure 7a). Overall, the diorite samples have a strong magnetization (Figure 7b). The majority of diorite samples have a steep HCC/high temperature component (HTC) (78.6° ± 2.0°, $n = 65$; Figure 7h) that is typically removed by 30 mT for most of the samples with a few retaining about 5% of their ChRM up to 80 mT (an example shown in Figure 8c). A LCC/low-temperature components (LTC) with an intermediate inclination (40.4° ± 5.0°; $n = 32$; Figure 7i) can be resolved for 32 of the diorite samples. This component is typically removed by ∼10 mT or 440°C (an example shown in Figure 8d). A few samples display more complex demagnetization behavior, with either poorly resolved ChRMs or with multiple components that can be resolved. The most interesting of these is sample U1480G-69R-5W, 24 cm (Figure 8e), which was collected just 54 cm from the base of the 37.45-m-thick diorite intrusion. This sample has three components (see the green arrows in Figure 8e): (a) a very LCC (less than about 8 mT) that is relatively steep and is interpreted as a drilling overprint, (b) an intermediate coercivity component (8–20 mT) that has a very shallow inclination (<20°) and is interpreted to be a geologically recent chemical or thermal overprint, and (c) the HCC (>20 mT) steep component, which is interpreted to be the ChRM acquired when the diorite was emplaced. The proximity of this sample to underlying higher porosity (22%–45%) sediments (Figure 2i) may have exposed it to heated fluids, that reset the magnetization of magnetic minerals with relatively low coercivity.

The Unit V sediments above and below the diorite have weaker magnetizations (Figure 7b) and more complex demagnetization behavior. Most samples are characterized by a shallow LCC that is typically removed by ∼5–10 mT. The HCC/HTC inclinations of 6 samples from Subunit Va and 7 samples from Subunit Vc average to 4.2° ± 3.7° (Figure 7g; an example shown in Figure 8g) and −10.8° ± 6.9° (Figure 7j; examples shown in Figures 8h–8j), respectively (Table S2). Generally, AF demagnetization at 20–25 mT or TD at 250°C removed ∼90% of the NRM, this indicates that these isolated HCCs/HTCs are recently acquired overprints rather than a primary magnetization. The remaining weak magnetizations above 20–25 mT or 250°C have erratic demagnetization behavior. One sample from Subunit Va was not included in the average as we consider it an outlier (with inclination of −19.7°). Two Subunit Va samples and three Subunit Vc samples have intermediate-to-steep HCCs/HTCs with inclinations of 47.1° ± 3.7° (Figure 7g; an example shown in Figures 8f) and 65.0° ± 5.6° (Figure 7j), respectively.

#### 3.2.3. Unit IV (Basalt Flows and Volcaniclastic Breccia, 1327.18–1349.80 Mbsf)

In Unit IV, we measured 6 samples from the lower basalt interval, 6 samples from the upper basalt interval, 3 samples from the volcaniclastic breccia separating the basalts, and 3 samples from the coarse tuffaceous sandstone at the base of the unit (Figure 7a). The demagnetization behavior of the 3 sandstone samples was too erratic but the remaining samples produced reliable results. The remaining 15 samples record a very consistent steep HCC/HTC (80.4° ± 2.7°; Figure 7f). Except for a few samples (an example shown in Figure 8k), most samples have a LCC or LTC (an example shown in Figure 8l) that is totally removed by AF at 15 mT or TD at 250°C, respectively.

#### 3.2.4. Unit III (Tuffaceous Silty Claystone; 1310.10–1327.18 mbsf)

We demagnetized 44 and 14 samples from Subunits IIIA and IIIB, respectively (Figure 7a). Besides the steep LCC/LTC that is likely a drilling-induced overprint, a stable but shallow HCC/HTC can be isolated, although a few samples are noisy. The HCC/HTC of 12 samples from Subunit IIIB have a mean inclination of −7.3° ± 3.5°

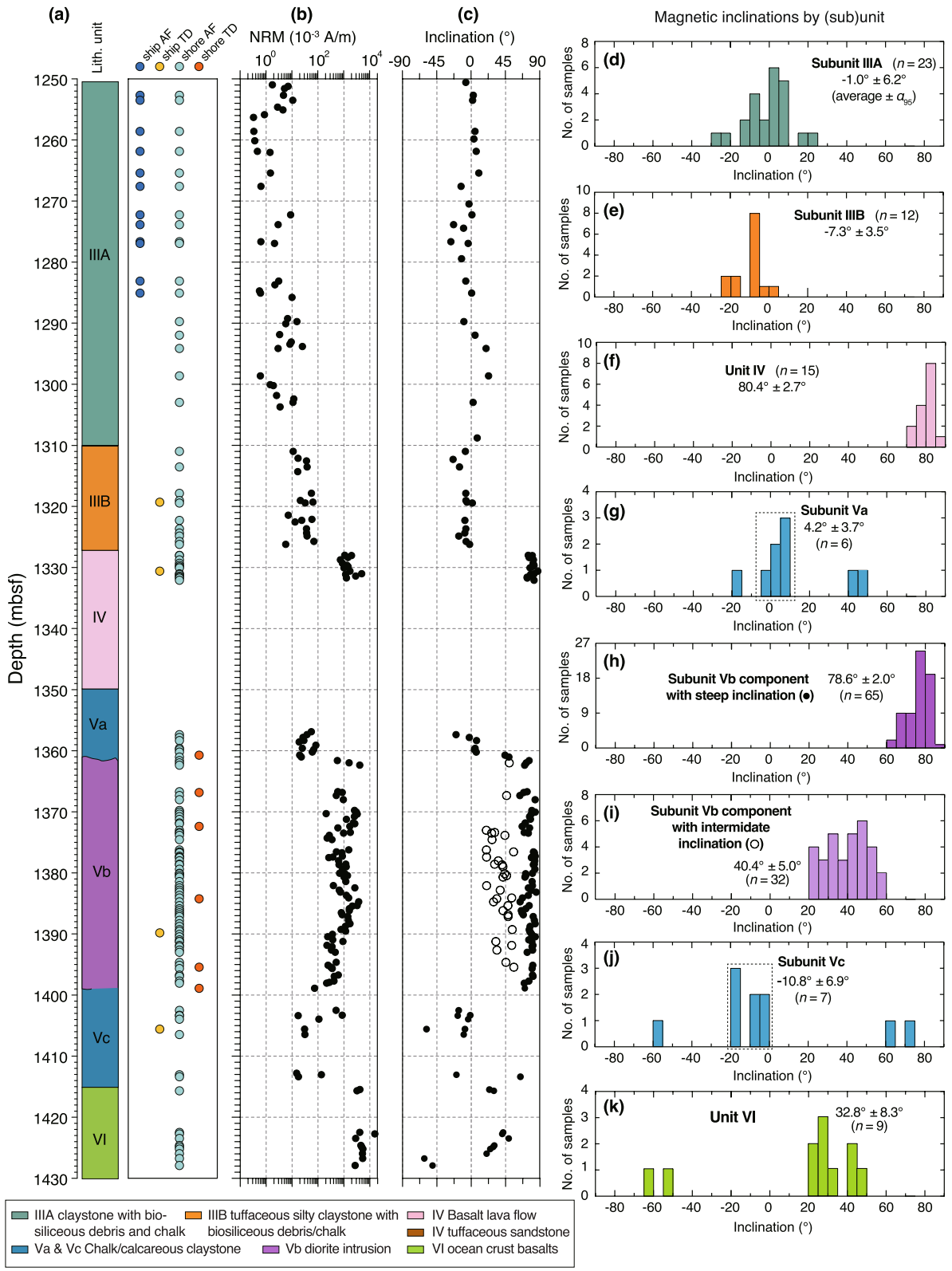


**Figure 7.**

(Figure 7e; examples shown in Figures 8m and 8n), whereas 23 samples from Subunit IIIA have a mean inclination of −1.0° ± 6.2° (Figure 7d; an example shown in Figure 8o).

### 3.3. SEM/EDS Observations

SEM observations focused on opaque, iron-bearing minerals, with the phase interpretation based on the habit, the EDS analyses, and the rock magnetic properties. Opaque minerals in the Unit III sediments are magnetite, mostly <20 μm (Figures 9a and 9b), which are tightly encapsulated by clay minerals, implying they are synsedimentary. Euhedral pyrite grains with altered/dissolved surfaces (Figure 9c) are widely present in sediments from Subunit IIIA but are rare in Subunit IIIB. In some case, the pyrite grain is almost completely dissolved with circular pyrite remnant rim left (Figure 9d). A significant feature for these sediments is the presence of large euhedral blocky crystals of barite, up to several tens of μm (Figure 9e). For the Unit IV basalt flows, large irregularly shaped ilmenite grains are present and a great number of titanomagnetite grains, characterized by honeycomb structure with a dominated parallel arrangement of the voids (or lamellae), are also observed in these samples (Figure 9f). In the Subunit Vb diorite, titanomagnetite with varying Ti content is generally present as large euhedral blocky crystals embedded in the plagioclase, whereas ilmenite generally occurs as laths crystals (Figure 9g). Occasionally, large dendritic magnetite grains (Figure 9h) are observed, indicating they have grown within rapidly cooling melts that are saturated with respect to iron (Shaar & Feinberg, 2013). The VI basaltic basement is dominated by plagioclase, clinopyroxene, and titanomagnetite, which generally occur as skeletal intergrowth of euhedral blocky crystals enclosed in a chlorite matrix, whereas magnetite also occasionally occurs as large (∼30 μm) euhedral blocky crystals (Figure 9i).

In the Subunit Va and Vc sediments, magnetite is identified as the major iron-bearing mineral and four typical modes of occurrence with altered appearance are identified. The first mode is characterized by dissolution voids with irregular shapes (generally <1 μm wide and 2–3 μm long; Figures 9j and 9k). Some particles exhibit a zonation with different Ti and Fe contents (Figure 9k). Generally, Ti content increases inward from the periphery with microvoids (Figure 9l). This suggests that the titanomagnetite underwent a phase transformation caused by dissolution. The second mode is relic magnetite that occurs as hollow crystals with a thin mantle, and some remnants inside (Figure 9m). The third mode is characterized by snowflake-shaped texture that is composed of many dendrites of magnetite radiating from the center outwards (Figure 9n), suggesting a nature of precipitation from iron-bearing hydrothermal fluids. The fourth mode is an intergranular texture (aggregates of disaggregated magnetite particles) that is characterized by pervasive alteration (Figure 9o), along with the presence of siderite and rhodochrosite aggregates. In some cases, the shape of the primary grain is still visible (inset, Figure 9o). This mixture of magnetite, siderite, and rhodochrosite suggests that the magnetite underwent pervasive dissolution with the precipitation of new phases. In addition, some ilmenite grains with smooth edges but etch pits and crevasses are also observed (Figure 9p). Another significant feature of the Subunit Va and Vc sediments is the presence of abundant chains of rhodochrosite filling the fractures of silicates (Figure 9q), with euhedral crystals of siderite, barite, as well as rhodochrosite aggregates also present (Figures 9r and 9s).

## 4. Discussion

### 4.1. Magnetic Carriers and Granulometry

Rock magnetic (Figures 2–6) and SEM/EDS (Figure 9) data aid in understanding the NRM acquisition mechanisms that produced the various magnetization components (Figures 7 and 8) in the studied samples. As indicated by these observations, the dominant magnetic carrier in Unit III sediments is SD/vortex state magnetite. Small amounts of other magnetic minerals (pyrite, hematite) are also present in several samples, especially in the upper portion of Subunit IIIA. However, the grain size of these magnetite grains decreases with depth, as demonstrated by the decreasing in $B_{cr}/B_c$ ratios and increasing in $M_{rs}/M_s$ ratios (Figures 2g and 2h), the trend toward the SD field in a Day-Dunlop plot (Figure 3q), and the distinct distributions in FORC diagrams

**Figure 7.** Paleomagnetic samples and data summary for all studied samples from lithostratigraphic Units III-VI, Hole U1480G. (a) Lithological (sub)units and paleomagnetic treatments. Ship AF and TD: alternating field and thermal demagnetization carried out onboard the *JOIDES Resolution* during Expedition 362; Shore AF and TD: AF and TD carried out postexpedition. Downhole variations of (b) NRM intensity, (c) inclinations of the remanence components. Except for Subunit Vb with two components (one with steep direction [●], and another one with intermediate direction [○]), only one stable remanence component was isolated for the other (sub) units. (d-k) Histograms for inclinations by (sub)unit with statistical results (average ± $\alpha_{95}$) using the statistical method of Arason and Levi (2010).

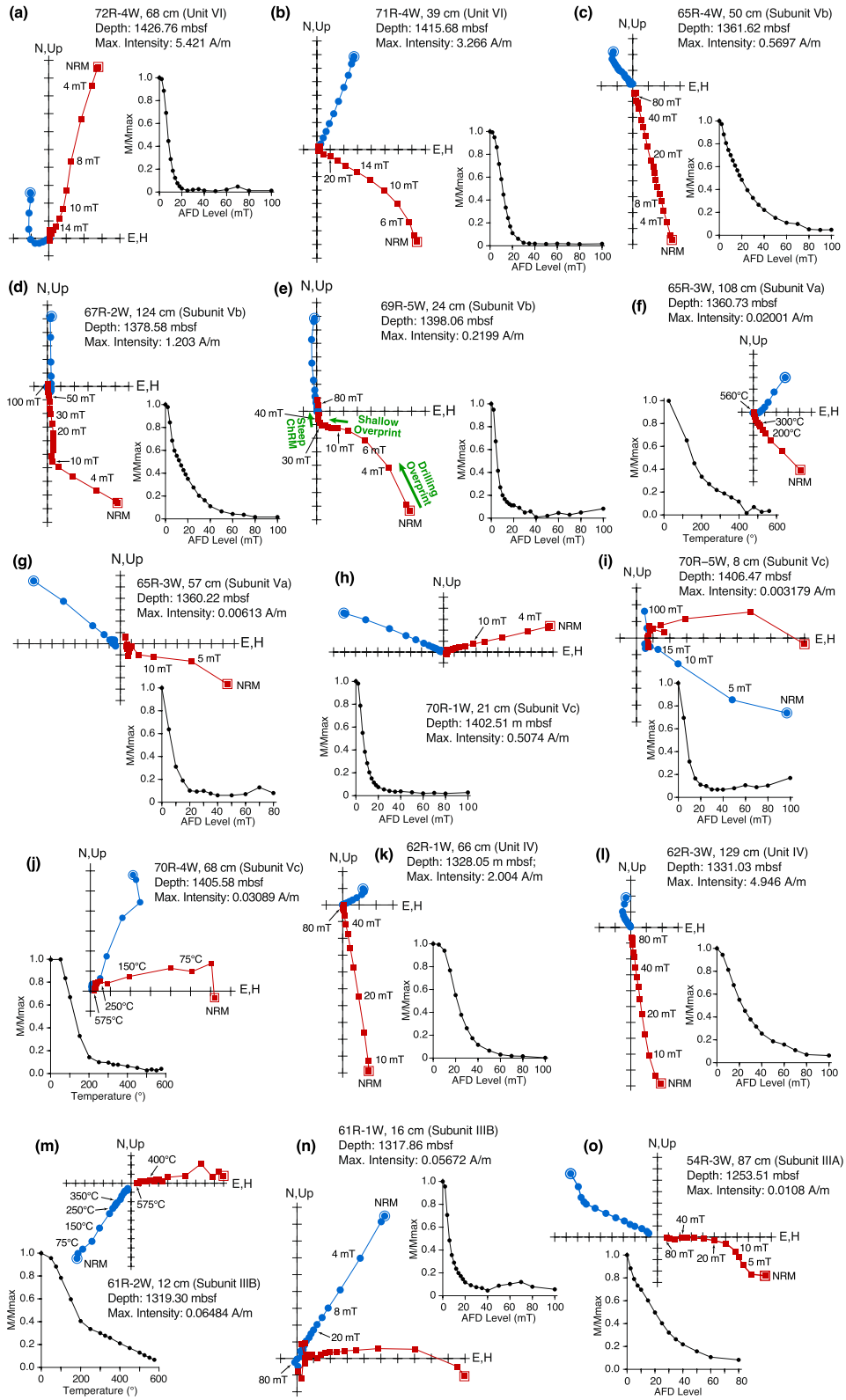


**Figure 8.** Orthogonal demagnetization diagrams for representative samples from different lithostratigraphic (sub)units after stepwise thermal and alternating field demagnetization. Blue dots and red squares indicate horizontal and vertical plane projections, respectively. Insets show magnetization decay with increasing AF or temperature, the magnetization M is normalized by its maximum intensity.

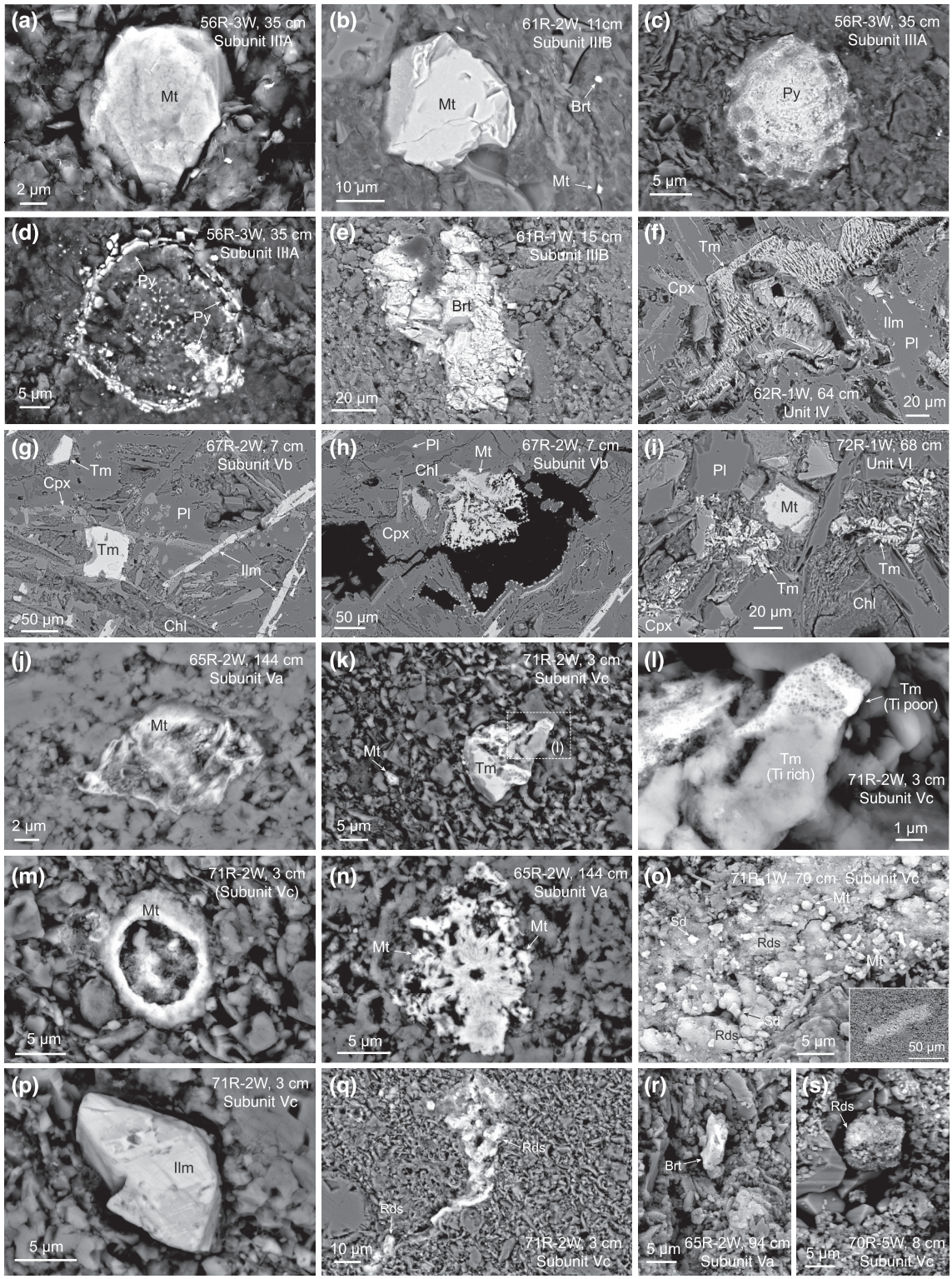


**Figure 9.**

(Figures 4a–4e). In addition, pyrite with etched dissolution pits (Figure 9c), even relics of dissolved pyrite (Figure 9d) are present in the upper level of Subunit IIIA and disappears gradually, possibly due to further dissolution, downward through Subunit IIIB.

For the Unit IV basalts, Subunit Vb diorite, and Unit VI basalts, titanomagnetite with varying Ti content is the predominant magnetic carrier, as revealed by the observed Curie temperature of ~550°C (Figure 5), which is lower than that of stoichiometric magnetite (~580°C; Dunlop & Özdemir, 1997). The presence of titanomagnetite is also indicated by their distinctive low-temperature behavior (Figure 6). Those titanomagnetite particles are coarse grained, mostly in the vortex state/MD grain size range, as highlighted by their hysteresis loops, Day-Dunlop plot distribution (Figure 3), FORC diagrams (Figure 4), and SEM/EDS observations (Figure 9). While abundant ilmenite grains are also present (Figure 9), they do not contribute to the NRM because of their paramagnetic nature.

The dominant magnetic carrier in Subunit Va and Vc sediments is magnetite. However, the absence of a Verwey transition at 120 K for both ZFC/FC and RT-SIRM cooling/heating curves suggests they could be possibly oxidized or not stoichiometric (Aragón et al., 1985; Jackson & Moskowitz, 2021; Muxworthy & McClelland, 2000; Zhang, Appel, Stanjek, et al., 2021; Özdemir & Dunlop, 2010). The mixing lines of Dunlop (2002) suggest that Subunit Va and Vc sediments contain a bimodal grain size distribution of small SD grains and 7–10 nm SP grains in large volume proportions of SP (Figure 3q). This is also highlighted by their considerably higher $\chi_{fd}$% values (Figure 2b), which is sensitive to the abundance of fine-grained SP/SD magnetic particles (e.g., Dearing et al., 1996; Maher & Thompson, 1999). The SP grains do not contribute to the NRM but have a large influence on the hysteresis properties of the samples (Figure 3) and FORC distribution (Figure 4). These finer-grained magnetic grains may be inherited from dissolution-reprecipitation reactions of the primary magnetite particles, which have been pervasively dissolved, with small relict magnetite grains left and/or some fine magnetite grains precipitated, as demonstrated by the SEM observations (Figure 9).

To summarize, the magnetic mineral assemblage for all the sedimentary samples is dominated by magnetite with varying particle size and concentration. Vortex state/MD (Ti-rich) titanomagnetite dominates all the igneous rocks including basalt and diorite. The magnetite seen in sediments is mainly detrital and has been pervasively altered in Subunits Va and Vc to a mixture of SD grains with a relatively large proportion of grains in the SP range. A small amount of hematite is also present in Subunits IIIA and IIIB, which is also supported by the reddish mottled character of some of the Subunit IIIB sediments (e.g., Figures 28 and 58 in McNeill et al., 2017).

### 4.2. NRM Components: Primary or Overprints?

Paleomagnetic analysis shows that most of the studied samples have multiple, well-resolved NRM components, apart from the steep, low-coercivity, drilling-induced overprint. The nature and fidelity of the various NRM components is examined below.

**Figure 9.** Backscattered electron (BSE) micrographs for representative samples from different lithological (sub)units showing the occurrence of major opaque minerals. (a–b) Magnetite (Mt) particles of detrital, synsedimentary origin, are ubiquitous in Unit III sediments. (c) Euhedral pyrite (Py) grains with etch pits, and (d) circular pyrite relics in Subunit IIIA sediments, suggesting they have undergone partially or pervasively alteration/dissolution, respectively. (e) Large blocky barite (Brt) crystals are widespread in Unit III sediments, highlighting the occurrence of hydrothermal fluids. (f) Large irregularly shaped ilmenite (Ilm) grains in Unit IV basalt flows, where titanomagnetite (Tm) with honeycomb texture also widely occurs. (g) Blocky titanomagnetite (Tm) crystals and ilmenite (Ilm) laths embedded plagioclase (Pl) and clinopyroxene (Cpx) in Sunbunit Vb diorite, with occasional presence of large dendritic magnetite (Mt) grains (h). (i) Skeletal crystals of titanomagnetite (Tm) with blocky magnetite (Mt) crystals enclosed by chlorite (Chl) matrix in Unit VI basalt basement. (j) Magnetite (Mt) grain with large irregular dissolution voids in Subunit Va sediments. (k) Large titanomagnetite (Tm) particles with dissolution voids in Subunit Vc sediments. (l) Enlarged view of the periphery portion of the particle in panel k showing zonation with different Ti and Fe contents. The bright periphery with microvoids have relatively lower (~4–5 wt%) Ti than the dark part (~20 wt% Ti), suggesting it has undergone a phase transformation. (m) Magnetite (Mt) hollow with some remnant inside in Subunit Vc sediments. (n) Snowflake-shaped magnetite (Mt) particles composed of many dendrites of magnetite radiating from the center outwards in Subunit Va sediments, indicating an origin of hydrothermal precipitation. (o) Disaggregated magnetite particle with visible original morphology (inset), along with the presence of siderite (Sd) and rhodochrosite (Rds) aggregates in Subunit Vc sediments. (p) Ilmenite (Ilm) grains with smooth edges but contain etch pits and crevasses in Subunit Vc sediments. (q) Rhodochrosite (Rds) chains filling the fracture of silicates in Subunit Vc sediments. (r) Euhedral crystals of barite (Brt) and (s) rhodochrosite (Rds) aggregates are ubiquitous in Subunit Va and Vc sediments. Panel e, o, r and s were imaged on bulk samples, and the others imaged on thin sections.

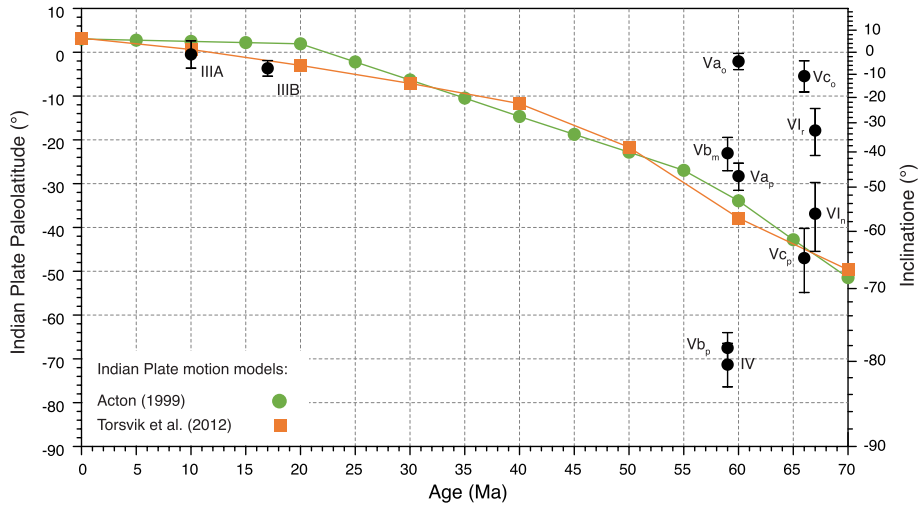


**Figure 10.** Comparison of paleolatitudes estimated from Hole U1480G Units III–VI versus those predicted from Indian Plate motion models (Acton, 1999; Torsvik et al., 2012). The dark dots represent average paleolatitudes estimated according to the corresponding average inclinations of different (sub)units or components shown in Figure 7; the upper and lower bars represent 95% confidence levels. Subscripts on Units III-VI are given as "o" for overprint, "p" for primary, "m" for mid-coercivity overprint component, "n" for normal polarity primary component, and "r" for reversed polarity primary component. Subunits IIIA and IIIB are given no subscript because they could be a primary or an overprint component, as discussed in the text. The highly altered nature of the Subunit IIIB sediments do, however, make it extremely probably that their magnetization is an overprint.

### 4.2.1. Unit VI Basement Basalt

Site U1480 is located very close to the boundary between marine magnetic anomalies C30n and C29r in the Wharton Basin (Figure 1a; Jacob et al., 2014). The C30n/C29r transition is dated at 66.3 Ma in the geomagnetic polarity timescale used during Expedition 362 (McNeill et al., 2017). In addition, the ocean crust basalts we recovered are constrained by microfossil ages to be younger than 67.4 Ma (Backman et al., 2019). Based on the ages of the sediments immediately above the basalts and the change in inclinations from a normal to a reversed polarity (Figure 8c), we infer that this transition corresponds to the Chron C30n/C29r reversal. These basement basalts are dominated by coarse-grained titanomagnetite, and most of them are well preserved (Figure 9). The stable HCC present in these basement basalts could be interpreted as the primary magnetization (Figures 7k and 8). Although the upper portion of Unit VI has a much shallower positive inclination (32.8° ± 8.3°, Figure 7k) than the expected one (~64°, Figure 10), this could merely be caused by secular variation that was recorded by two lava flows extruded closely together in time rather than a secondary chemical overprint. Even if the Unit VI basalts do record a Late Cretaceous primary magnetization, they also contain evidence of moderate alteration, as seen in the saussuritization of plagioclase and the alteration of pyroxene to chlorite (Figure 9). This is also supported by the brownish color and the occurrence of mineral-filled fractures in basaltic basement samples (McNeill et al., 2017). Thus, even though we do not think the basalts have been overprinted by fluid migration along a pre-décollement, they have at least been exposed to diagenetic fluids.

### 4.2.2. Unit V Sedimentary Package Intruded by Diorite

The Subunit Vb diorite has an age of 58.93 ± 0.15 Ma, with an expected inclination of ~51° at the drill site following the Indian Plate motion model of Acton (1999). Most diorite samples have very steep HCCs/HTCs (78.6° ± 2.0°, Figure 7h), much higher than the expected inclination (Figure 10). It is interpreted to be a primary Eocene-age magnetization, which just happens to be steep like the drilling overprint. Sample U1480G-69R-5W, 24 cm (Figure 8e) provides an example of these two steep components being independent magnetizations with similar directions; the sample has both a steep low coercivity drilling overprint and a steep high coercivity primary component, which are separated by an intermediate coercivity shallow component. If the drilling overprint had affected the full coercivity spectrum, the intermediate component would have also been overprinted. We suggest that the shallow component is better recorded in this diorite sample than in other diorite samples because it is the sample nearest the contact with Subunit Vc, which has a much higher porosity than the diorite (Figure 2i) allowing

circulation of warm fluids that could have altered the intermediate coercivity magnetic minerals along the Subunits Vc/Vb contact.

Many of the diorite samples that have recorded the steep HCC also record an intermediate direction (40.4° ± 5.0°, Figure 7i) and a few samples record only this intermediate direction. The origin of this component is more complicated to explain as it is not as shallow as some of the overprints in the sedimentary units. We suspect it was acquired as a secondary chemical remanent magnetization (CRM) since the Miocene and that the coercivity overlaps somewhat with both the drilling overprint and the steep HCC.

The secondary magnetization is more obvious in the more porous sedimentary units. The sediments of Subunits Va and Vc have ages of ∼60 Ma and ∼67 Ma, respectively (Backman et al., 2019), at which time the inclinations predicted by the Indian Plate motion model of Acton (1999) are ∼53° and 64°, respectively (Figure 10). This large discrepancy between the very shallow measured (4.2° ± 3.7° and −10.8° ± 6.9°, Figures 7g and 7j) and predicted inclinations (Figure 10) cannot be explained by sediment compaction. Considering the pervasive alteration/dissolution of magnetite seen in SEM images (Figure 9), we attribute the shallow components to overprints. A few Subunit Va and Vc samples have higher coercivity, intermediate-to-steep components (Figures 7g–7j), whose directions are close to the expected inclinations (Figure 10), suggesting that these samples may retain a primary magnetization.

#### 4.2.3. Unit IV Basalt Flows and Volcaniclastic Breccia

The age of the basalt flows in Unit IV are estimated to be at least ∼58 Ma (Backman et al., 2019). Given the reversed polarity of the basalt flow, we infer that they were emplaced during Chron C25r. At that time, the expected inclination for Site U1480 is ∼49°. The measured HCC/HTC inclinations are, however, very steep (80.4° ± 2.7°, Figure 7f). The demagnetization diagrams for most of these samples are very linear over a coercivity spectrum from 6 mT up to 80 to even 100 mT. This is surely a primary magnetization, which also happens to have a steep direction. A single lava flow or even a few flows are insufficient to use to compare to an expected paleomagnetic pole, because secular variation is not average by only a few virtual geomagnetic poles. Basically, like the basalts of Unit VI and the diorite of Subunit Vb, these basalts retain a primary magnetization because they are not porous and so have not been partially or totally remagnetized like the sedimentary units that underly or overly them.

#### 4.2.4. Unit III Tuffaceous Silty Claystone

All the tuffaceous silty claystone samples were collected above the 1326.55 mbsf hiatus identified in McNeill et al. (2017) and Backman et al. (2019). Therefore, these sediments are young (17–9.3 Ma) with shallow expected inclinations (Figure 10). For example, the 20 Ma expected inclination for Site U1480 is −6° (Torsvik et al., 2012). This suggests that the HCC/HTC (−1.0° ± 6.2°, and −7.3° ± 3.5°, Figures 7d and 7e) could represent either the primary magnetization or the shallow overprint seen in Subunits Va and Vc or a combination of both. However, based on the rock magnetic analyses (Figures 2–6), magnetite is the predominant magnetic carrier, which are mostly well preserved in SEM images (Figure 9). It is therefore possible that these shallow HCC/HTC represent the primary magnetization.

In summary, paleomagnetic analysis of 154 samples from the older portion of Site U1480 in the Wharton Basin shows that several lithostratigraphic units retain a primary magnetization. Specifically, the basement basalts of Unit VI (∼66 Ma), most of the diorite samples of Unit V (∼59 Ma), and the basalt flows of Unit IV (∼58 Ma) are characterized by relatively steep magnetization directions that we interpret as the primary magnetization. A remarkable observation is that the sediments at the top and bottom of Unit V have shallow average inclinations of 4.2° and −10.8°, respectively. These are clearly overprints given that the sediments are between ∼60 Ma and 66 Ma, during which time Site U1480 was located between 35°S and 45°S, with expected inclinations >50°.

### 4.3. Timing of Remagnetization

The timing of acquisition of the shallow overprint components provides important clues to the possible remagnetization mechanisms. This timing can be relatively well constrained owing to the rapid northward motion of the Indian plate over most of the past 70 Ma, during which the paleolatitude of Site U1480 has changed from about 50°S to 3°N. To estimate magnetization ages, the observed paleolatitudes obtained from the paleomagnetic

inclinations for Units III–VI are compared with the expected paleolatitude for Site U1480 (Figure 10) based on the Indian Plate APWP of Acton (1999) and Torsvik et al. (2012). Site U1480 had a paleolatitude of between 50°S and 30°S between 70 Ma and 55 Ma, which equates to inclinations of between 67° and 49°. Thus, intermediate to steep inclinations would be expected for Units IV–VI if they retained a magnetization that was acquired during or shortly after deposition, as is typically the case for sediments that have not been thermally or chemically altered.

This comparison shows that the paleolatitudes estimated from the primary components for the diorite intrusion of Subunit Vb, the basalts of Units IV and VI, and the sediments of Subunits Va and Vc (Figure 10) are relatively consistent with the expected paleolatitudes, although secular variation surely is not averaged out by (Sub)units IV, Vb, and VI. On the other hand, the exceedingly shallow overprint directions of Subunit Va and Vc sediments imply the magnetization was acquired a long time after deposition. The 95% confidence limits on the paleolatitudes of these units permit acquisition of the overprint anytime since the early Oligocene (Figure 10).

As discussed above, the shallow directions from the Subunit IIIB sediments may represent either a primary or secondary magnetization. Based on directions alone, the timing of the magnetization of Subunit IIIB cannot be determined. The very mottled reddish to brownish color of the sediments indicate Subunit IIIB has been highly altered (e.g., see McNeill et al. (2017) figures F28 and F58). Indeed, the reddish splotches are referred to as "redox spots (diagenetic spots whose origin awaits further analysis)." Reddish splotches occurring along faults in Section U1480G-61R-1 are interpreted as possibly originating from focused "advection of diagenetic subsurface fluids" (McNeill et al., 2017). Given the visible alteration of the sediment, it seems probable that the shallow direction in Subunit IIIB is an overprint and the timing of the overprint is at least younger than the age of deposition (17–9.3 Ma).

Assuming the DISSDI model holds, the timing of the overprint can be further constrained by sediment accumulation rates and thermal modeling. For instance, if diagenesis and associated remagnetization is driven by deep burial by the Nicobar Fan sediments, the pre-fan sediments, including Unit V and Unit III, would not have been buried deeper than 600 m until after about 6 Ma and deeper than 1200 m by only about 1.8 Ma (Backman et al., 2019). Furthermore, thermal modeling results indicated that temperature increases related to rapid burial reach their highest values at Site U1480 in only the past 100,000 years (Hüpers et al., 2017). Thus, the remagnetization most likely occurred quite recently and unlikely occurred more than a few million years ago.

### 4.4. Mechanisms of Remagnetization: Links With Alteration

Remagnetization can be caused by a variety of processes, such as thermoviscous resetting, chemical alteration by the introduction of fluids (e.g., orogenic, basinal, brines and mineralizing fluids), hydrocarbon generation deeper in the sediment, and burial diagenetic processes (see review by Elmore et al. (2012) for more details). Here, the Subunit Va and Vc sediments have quite different magnetization directions from the intruded basalt flows and diorite (Figures 7 and 10), which precludes a thermoviscous magnetization as the likely remagnetization mechanism. Rock magnetic analyses revealed the predominance of magnetite as the remanence carrier in these sediments. While SEM observations demonstrate that almost all of magnetite grains have suffered pervasive dissolution and alteration, with the presence of abundant stratabound barite and rhodochrosite patches and veins, and siderite (Figure 9), which are diagnostic minerals for hydrothermal processes (e.g., Griffith & Paytan, 2012; Rye, 2005). This suggests that chemical alteration caused by hydrothermal fluids is the most likely mechanism of remagnetization in these sediments.

The volcanogenic-rich Unit III sediment contains >20 wt% amorphous silica (McNeill et al., 2017), which constitutes an important reservoir of mineral-bound water available for release upon dehydration. Thermal modeling by Hüpers et al. (2017) revealed that rapid burial of these hemipelagic to pelagic sediments by the rapid deposition of ∼1,250 m of Nicobar Fan sediments and the subsequent increase in temperature resulted in amorphous silica dehydration reactions that introduced warm fluids and changed pore water chemistry in the deeper part of the stratigraphic section. These warm fluids could have migrated along structural and stratigraphic surfaces (e.g., unconformities, synsedimentary faults, and fractures) or interconnected porosity, and percolated into the Unit V sediments. Shipboard porosities in Hole U1480G indicate the sediments below 1300 mbsf generally have porosities of 20%–60% whereas the igneous units have porosities of 4%–16% (McNeill et al., 2017; Figure 2i). Magnetite is unstable under elevated porewater silica concentration and will dissolve rapidly to release $Fe^{2+}$ (Florindo et al., 2003). Fine-grained magnetite particles were then precipitated and

embedded in the pore space. Such magnetite dissolution/precipitation processes may be illustrated by the following chemical reactions (Otake et al., 2010):

$$Fe_3O_{4(mt)} + 2H^+_{(aq)} + 2H_2O \leftrightarrow Fe^{2+}_{(aq)} + 2Fe(OH)_{3(aq)} \quad (1)$$

$$Fe^{2+}_{(aq)} + 4/3H_2O \leftrightarrow 1/3Fe_3O_{4(mt)} + 2H^+_{(aq)} + 1/3H_{2(g)} \quad (2)$$

The dissolution, which is most pervasive under reducing conditions, resulted in the formation of microvoids, grain-surface etching, and cracking of the Fe-Ti-oxide grains (Figure 9). It is reported that $Fe^{2+}$ may be substituted by Mg, Mn, Zn, and Ni, and $Fe^{3+}$ by Al, V and Cr during the precipitation of magnetite (e.g., Lindsley, 1991; Nadoll et al., 2014). Such cation substitution, together with the surface oxidation, not only suppress the Verwey transition of magnetite (Figure 6), could also decrease its saturation magnetization, resulting in less significant magnetic interactions (Rebodos & Vikesland, 2010), as demonstrated by their FORC distribution.

In addition, temperature was estimated to be ~59°C at the base of Unit III by Hüpers et al. (2017). Such a temperature (~50–110°C) facilitates the smectite to illite conversion reaction (Katz et al., 1998, 2000; Weibel, 1999), which would also liberate the iron required for the formation of magnetite (e.g., Aubourg et al., 2012; Kars et al., 2021). Iron released during the smectite-illite conversion that reaches completion by ~120–150°C (Vrolijk, 1990) would partly remain in situ in the clay aggregates, where it would crystallize as fine-grained magnetite. Therefore, the byproduct of illite formation to some extent also contributed to overprinting the primary magnetization. As demonstrated by the pervasive alteration of the pre-existing magnetite particles (Figure 9), however, it is plausible that hydrothermal alteration is the dominant mechanism responsible for overprinting the primary magnetization.

Direct crystallization of magnetite from the hydrothermal fluids and smectite to illite conversion can also explain the mixture of SP/SD magnetite grains in these sediments as inferred from the considerably higher $\chi_{fd}$% values (Figure 2b), hysteresis data (Figure 3). Among them, the SD grains with a high alignment efficiency recorded the contemporaneous paleomagnetic signal through CRM, leaving a shallow overprint in these sediments. This evidence suggests that the paleomagnetic directions are consistent with the dehydration occurring in the higher porosity units below the thick Nicobar Fan sediments (Hüpers et al., 2017; McNeill et al., 2017). In contrast, the intruded basalt flow and diorite have much lower porosity (Figure 2i) and permeability, largely insulating them from alteration, and so their primary magnetization mostly survived.

The warm fluids that resulted from mineral dehydration reactions not only caused the magnetic (iron-bearing) mineral alteration/dissolution, but also altered the properties of the sediments long before they reach the subduction zone. Hüpers et al. (2017) postulated that the diagenetic strengthening of the sediments involved in the formation of the boundary fault led to the large magnitude of the Sumatra-Andaman 2004 earthquake. This implies that the paleomagnetic overprints observed in pre-fan sediments are connected to seismogenic diagenetic strengthening. It has been reported that other subduction zones (e.g., Makran, Cascadia, and southern Lesser Antilles) resembling the Sumatran Zone have thick input sediments or high temperatures or both, where the thickness and thermal state of sediments are all affected by input of submarine fan sequences (Hüpers et al., 2017; Smith et al., 2013). This study suggests that the remagnetization observed for the Sumatra subduction zone may be typical in similar subduction zones, and that paleomagnetic and rock magnetic studies of input sediments may provide important clues on the evolution of subduction margins and the chemical/physical conditions that may contribute to the generation of large, tsunamigenic earthquakes.

## 5. Conclusions

Together, rock magnetic and paleomagnetic analyses, and SEM/EDS observations of pre-fan sediments cored during IODP Expedition 362 offshore Sumatra reveal that the lower portion of pre-fan pelagic sediments have been partially to fully remagnetized. These observations support the DISSDI hypothesis that suggests that warm fluids are generated from mineral dehydration reactions that are driven by rapid burial of older hemipelagic to pelagic sediments by the thick Nicobar Fan sediments. The remagnetization led to CRMs with much shallower inclinations than expected for the Paleocene to Late Cretaceous sediments based on the motion history of the Indian plate. The warm fluid flow resulted in pervasive dissolution/alteration of the pre-existing detrital

magnetite, while the elevated burial temperature facilitated the smectite to illite conversion reaction. These chemical reactions resulted in the formation of submicron to micron-sized magnetite as the dominant remanence carrier. The paleomagnetic directions of the remagnetized sediments are consistent with the alteration and diagenetic strengthening occurring sometime after Site U1480 on the Indian plate had moved northward and into the vicinity of the equator, which could be anytime since the early Oligocene. The rapid thickening of the sedimentary sequence at U1480, however, took place mainly from 9 to 2 Ma. If this thickening was the driver of the diagenetic event that caused the overprint, then the overprint is probably less than a few million years old.

## Data Availability Statement

Shipboard paleomagnetic data of discrete samples measured on the *JOIDES Resolution* during the IODP Expedition 362 are available on the Zenodo database (McNeill et al., 2020). Post-cruise paleomagnetic and rock magnetic data collected for this study can be found at Zenodo repository (Yang et al., 2024).

**Acknowledgments**
This research used data and samples provided by the International Ocean Discovery Program (IODP). We thank the Expedition 362 scientists, the JRSO technical staff, and the Siem Offshore crew of the *JOIDES Resolution* for making this expedition such a success. We also thank Weiwei Chen for her assistance at the Paleomagnetism facility of the State Key Laboratory of Marine Geology, Tongji University. We would like to thank Yan Zhang, Xinwen Cao, Liqin Yan for assistance with low-temperature magnetic measurements, Yuhang Zhang for thin section preparation, Xi Ma, Lihua Ding and Xiuli Yan for assistance with SEM/EDS observations. This manuscript has benefited from the constructive comments of Erwin Appel and Liao Chang. TY received support from IODP-China and the National Natural Science Foundation of China (NSFC, Grant 41874105). KP and GA received support from the IODP JRSO (NSF grant OCE1326927). KP also received laboratory support from a USSSP postexpedition grant. XZ received support from the NSFC (Grants 91628301, 91528302, 41674069) and U.S. National Science Foundation (Grant EAR-1250444).

## References

Acton, G. D. (1999). Apparent polar wander of India since the Cretaceous with implications for regional tectonics and true polar wander. In T. Radhakrishna & J. D. A. Piper (Eds.), *The Indian subcontinent and Gondwana: A palaeomagnetic and rock magnetic perspective. Memoir geological Society of India* (Vol. 44, pp. 129–175). Geological Society of India.

Acton, G. D. (2011). ZPLOTIT software users' guide, version 2011-01. [Computer software manual]. *Paléomag*. Retrieved from http://paleomag.ucdavis.edu/softwareZplotit.html

Ammon, C. J., Ji, C., Thio, H. K., Robinson, D., Ni, S., Hjorleifsdottir, V., et al. (2005). Rupture process of the 2004 Sumatra-Andaman earthquake. *Science*, *308*(5725), 1133–1139. https://doi.org/10.1126/science.1112260

Appel, E., & Soffel, H. (1985). Domain state of Ti-rich titanomagnetites deduced from domain structure observations and susceptibility measurements. *Journal of Geophysics*, *56*(1), 121–132.

Aragón, R., Buttrey, D., Shepherd, J. P., & Honig, J. M. (1985). Influence of nonstoichiometry on the Verwey transition. *Physical Review B*, *B31*(1), 430–436. https://doi.org/10.1103/physrevb.31.430

Arason, Þ., & Levi, S. (2010). Maximum likelihood solution for inclination-only data in paleomagnetism. *Geophysical Journal International*, *182*(2), 753–771. https://doi.org/10.1111/j.1365-246x.2010.04671.x

Aubourg, C., Pozzi, J.-P., & Kars, M. (2012). *Burial, claystones remagnetization and some consequences for magnetostratigraphy*. (Vol. 371, pp. 181–188). Geological Society Special Publication. https://doi.org/10.1144/sp371.4

Backman, J., Chen, W., Kachovich, S., Mitchison, F., Petronotis, K., Yang, T., & Zhao, X. (2019). Data report: Revised age models for IODP sites U1480 and U1481, expedition 362. In L. C. McNeill, B. Dugan, & K. E. Petronotis (Eds.), *Sumatra subduction zone. Proceedings of the International Ocean Discovery Program* (Vol. 362). International Ocean Discovery Program. https://doi.org/10.14379/iodp.proc.362.202.2019

Briggs, R. W., Sieh, K., Meltzner, A. J., Natawidjaja, D., Galetzka, J., Suwargadi, B., et al. (2006). Deformation and slip along the Sunda megathrust in the great 2005 Nias-Simeulue earthquake. *Science*, *311*(5769), 1897–1901. https://doi.org/10.1126/science.1122602

Childress, L. B., Acton, G. D., Percuoco, V. P., & Hastedt, M. (2024). The LILY database: Linking lithology to IODP physical, chemical, and magnetic properties data. *Geochemistry, Geophysics, Geosystems*, *25*(2), e2023GC011287. https://doi.org/10.1029/2023GC011287

Church, N., Feinberg, J. M., & Harrison, R. (2011). Low-temperature domain wall pinning in titanomagnetite: Quantitative modeling of multidomain first-order reversal curve diagrams and AC susceptibility. *Geochemistry, Geophysics, Geosystems*, *12*(7), Q07Z27. https://doi.org/10.1029/2011GC003538

Day, R., Fuller, M., & Schmidt, V. A. (1977). Hysteresis properties of titanomagnetites: Grain-size and compositional dependence. *Physics of the Earth and Planetary Interiors*, *13*(4), 260–267. https://doi.org/10.1016/0031-9201(77)90108-x

Dean, S. M., McNeill, L. C., Henstock, T. J., Bull, J. M., Gulick, S. P. S., Austin, J. A., Jr., et al. (2010). Contrasting décollement and prism properties over the Sumatra 2004–2005 earthquake rupture boundary. *Science*, *329*(5988), 207–210. https://doi.org/10.1126/science.1189373

Dearing, J. A., Dann, R. J. L., Hay, K., Lees, J. A., Loveland, P. J., Maher, B. A., & O'Grady, K. (1996). Frequency-dependent susceptibility measurements of environmental materials. *Geophysical Journal International*, *124*(1), 228–240. https://doi.org/10.1111/j.1365-246x.1996.tb06366.x

Dunlop, D. J. (2002). Theory and application of the Day plot ($M_{rs}/M_s$ versus $H_{cr}/H_c$): 1. Theoretical curves and tests using titanomagnetite data. *Journal of Geophysical Research*, *107*(B3), 2056. https://doi.org/10.1029/2001JB000486

Dunlop, D. J., & Özdemir, Ö. (1997). *Rock magnetism: Fundamentals and frontiers*. Cambridge University Press.

Elmore, R. D., Muxworthy, A. R., & Aldana, M. (2012). Remagnetization and chemical alteration of sedimentary rocks. *Geological Society, London, Special Publications*, *371*(1), 1–21. https://doi.org/10.1144/sp371.15

Fabian, K. (2003). Some additional parameters to estimate domain state from isothermal magnetization measurements. *Earth and Planetary Science Letters*, *213*(3–4), 337–345. https://doi.org/10.1016/s0012-821x(03)00329-7

Florindo, F., Roberts, A. P., & Palmer, M. R. (2003). Magnetite dissolution in siliceous sediments. *Geochemistry, Geophysics, Geosystems*, *4*(7), 1053. https://doi.org/10.1029/2003GC000516

Geersen, J., McNeill, L., Henstock, T. J., & Gaedicke, C. (2013). The 2004 Aceh-Andaman earthquake: Early clay dehydration controls shallow seismic rupture. *Geochemistry, Geophysics, Geosystems*, *14*(9), 3315–3323. https://doi.org/10.1002/ggge.20193

Griffith, E. M., & Paytan, A. (2012). Barite in the ocean–occurrence, geochemistry and palaeoceanographic applications. *Sedimentology*, *59*(6), 1817–1835. https://doi.org/10.1111/j.1365-3091.2012.01327.x

Harrison, R. J., & Feinberg, J. M. (2008). FORCinel: An improved algorithm for calculating first-order reversal curve distributions using locally weighted regression smoothing. *Geochemistry, Geophysics, Geosystems*, *9*(5), Q05016. https://doi.org/10.1029/2008GC001987

Hirt, A. M., Banin, A., & Gehring, A. U. (1993). Thermal generation of ferromagnetic minerals from iron-enriched smectites. *Geophysical Journal International*, *115*(3), 1161–1168. https://doi.org/10.1111/j.1365-246x.1993.tb01518.x

Hüpers, A., Torres, M. E., Owari, S., McNeill, L. C., Dugan, B., Henstock, T. J., et al. (2017). Release of mineral-bound water prior to subduction tied to shallow seismogenic slip off Sumatra. *Science*, *356*(6340), 841–844. https://doi.org/10.1126/science.aal3429

Jackson, M. J., & Moskowitz, B. (2021). On the distribution of Verwey transition temperatures in natural magnetites. *Geophysical Journal International*, *224*(2), 1314–1325. https://doi.org/10.1093/gji/ggaa516

Jacob, J., Dyment, J., & Yatheesh, V. (2014). Revisiting the structure, age, and evolution of the Wharton Basin to better understand subduction under Indonesia. *Journal of Geophysical Research: Solid Earth*, *119*(1), 169–190. https://doi.org/10.1002/2013jb010285

Just, J., & Kontny, A. (2012). Thermally induced alterations of minerals during measurements of the temperature dependence of magnetic susceptibility: A case study from the hydrothermally altered Soultz-sous-Forêts granite, France. *International Journal of Earth Sciences*, *101*(3), 819–839. https://doi.org/10.1007/s00531-011-0668-9

Kars, M., Köster, M., Henkel, S., Stein, R., Schubotz, F., Zhao, X., et al. (2021). Influence of early low-temperature and later high-temperature diagenesis on magnetic mineral assemblages in marine sediments from the Nankai Trough. *Geochemistry, Geophysics, Geosystems*, *22*(10), e2021GC010133. https://doi.org/10.1029/2021GC010133

Katz, B., Elmore, R. D., Cogoini, M., Engel, M. H., & Ferry, S. (2000). Associations between burial diagenesis of smectite, chemical remagnetization, and magnetite authigenesis in the Vocontian trough, SE France. *Journal of Geophysical Research*, *105*(B1), 851–868. https://doi.org/10.1029/1999jb900309

Katz, B., Elmore, R. D., Cogoini, M., & Ferry, S. (1998). Widespread chemical remagnetization: Orogenic fluids or burial diagenesis of clays? *Geology*, *26*(7), 603–606. https://doi.org/10.1130/0091-7613(1998)026<0603:wcrofo>2.3.co;2

Kirschvink, J. L. (1980). The least-squares line and plane and the analysis of palaeomagnetic data. *Geophysical Journal of the Royal Astronomical Society*, *62*(3), 699–718. https://doi.org/10.1111/j.1365-246x.1980.tb02601.x

Kosterov, A. (2003). Low-temperature magnetization and AC susceptibility of magnetite: Effect of thermomagnetic history. *Geophysical Journal International*, *154*(1), 58–71. https://doi.org/10.1046/j.1365-246x.2003.01938.x

Kosterov, A., Conte, G., Goguitchaichvili, A., & Urrutia-Fucugauchi, J. (2009). Low-temperature magnetic properties of andesitic rocks from Popocatepetl Stratovolcano, Mexico. *Earth Planets and Space*, *61*(1), 133–142. https://doi.org/10.1186/bf03352893

Kosterov, A. A., Sergienko, E. S., Kharitonskii, P. V., & Yanson, S. Y. (2018). Low temperature magnetic properties of basalts containing near ~TM30 titanomagnetite. *Izvestiya - Physics of the Solid Earth*, *54*(1), 134–149. https://doi.org/10.1134/s106935131801010x

Kuiper, K. F., Deino, A., Hilgen, F. J., Krijgsman, W., Renne, P. R., & Wijbrans, J. B. (2008). Synchronizing rock clocks of Earth history. *Science*, *320*(5875), 500–504. https://doi.org/10.1126/science.1154339

Lascu, I., Einsle, J. F., Ball, M. R., & Harrison, R. J. (2018). The vortex state in geologic materials: A micromagnetic perspective. *Journal of Geophysical Research: Solid Earth*, *123*(9), 7285–7304. https://doi.org/10.1029/2018jb015909

Lay, T., Kanamori, H., Ammon, C. J., Nettles, M., Ward, S. N., Aster, R. C., et al. (2005). The great Sumatra-Andaman earthquake of 26 December 2004. *Science*, *308*(5725), 1127–1133. https://doi.org/10.1126/science.1112250

Lindsley, D. H. (1991). *Oxide minerals: Petrologic and magnetic significance. Reviews in mineralogy* (Vol. 25). Mineralogical Society of America.

Lurcock, P. C., & Wilson, G. S. (2012). PuffinPlot: A versatile, user-friendly program for paleomagnetic analysis. *Geochemistry, Geophysics, Geosystems*, *13*(6), Q06Z45. https://doi.org/10.1029/2012GC004098

Maher, B. A., & Thompson, R. (1999). *Quaternary climates, environments and magnetism*. Cambridge University Press.

McNeill, L., Dugan, B., & Petronotis, K. (2016). *Expedition 362 scientific prospectus: The Sumatra subduction zone*. International Ocean Discovery Program. https://doi.org/10.14379/iodp.sp.362.2016

McNeill, L. C., Dugan, B., & Petronotis, K. E., & the Expedition 362 Scientists. (2017). Sumatra subduction zone. In *Proceedings of the International Ocean Discovery Program* (Vol. 362). International Ocean Discovery Program. https://doi.org/10.14379/iodp.proc.362.2017

McNeill, L. C., Dugan, B., Petronotis, K. E., Backman, J., Bourlange, S., Chemale, F., et al. (2020). IODP Expedition 362 Magnetic remanence (spinner). [Dataset]. *Zenodo*. https://doi.org/10.5281/zenodo.3754801

Muxworthy, A. R., & Dunlop, D. J. (2002). First-order reversal curve (FORC) diagrams for pseudo-single-domain magnetites at high temperature. *Earth and Planetary Science Letters*, *203*(1), 369–382. https://doi.org/10.1016/s0012-821x(02)00880-4

Muxworthy, A. R., & McClelland, E. (2000). Review of the low-temperature magnetic properties of magnetite from a rock magnetic perspective. *Geophysical Journal International*, *140*(1), 101–114. https://doi.org/10.1046/j.1365-246x.2000.00999.x

Nadoll, P., Angerer, T., Mauk, J. L., French, D., & Walshe, J. (2014). The chemistry of hydrothermal magnetite: A review. *Ore Geology Reviews*, *61*, 1–32. https://doi.org/10.1016/j.oregeorev.2013.12.013

Otake, T., Wesolowski, D. J., Anovitz, L. M., Allard, L. F., & Ohmoto, H. (2010). Mechanisms of iron oxide transformations in hydrothermal systems. *Geochimica et Cosmochimica Acta*, *74*(21), 6141–6156. https://doi.org/10.1016/j.gca.2010.07.024

Özdemir, Ö., Dunlop, D., & Moskowitz, B. (2002). Changes in remanence, coercivity and domain state at low-temperature in magnetite. *Earth and Planetary Science Letters*, *194*(3–4), 343–358. https://doi.org/10.1016/s0012-821x(01)00562-3

Özdemir, Ö., & Dunlop, D. J. (2003). Low-temperature behavior and memory of iron-rich titanomagnetites (Mt. Haruna, Japan and Mt. Pinatubo, Philippines). *Earth and Planetary Science Letters*, *216*(1–2), 193–200. https://doi.org/10.1016/s0012-821x(03)00481-3

Özdemir, Ö., & Dunlop, D. J. (2010). Hallmarks of maghemitization in low-temperature remanence cycling of partially oxidized magnetite nanoparticles. *Journal of Geophysical Research*, *115*(B2), B02101. https://doi.org/10.1029/2009JB006756

Passier, H. F., de Lange, G. J., & Dekkers, M. J. (2001). Magnetic properties and geochemistry of the active oxidation front and the youngest sapropel in the eastern Mediterranean Sea. *Geophysical Journal International*, *145*(3), 604–614. https://doi.org/10.1046/j.0956-540x.2001.01394.x

Pike, C. R., Roberts, A. P., & Verosub, K. L. (1999). Characterizing interactions in fine magnetic particle systems using first order reversal curves. *Journal of Applied Physics*, *85*(9), 6660–6667. https://doi.org/10.1063/1.370176

Rebodos, R. L., & Vikesland, P. J. (2010). Effects of oxidation on the magnetization of nanoparticulate magnetite. *Langmuir*, *26*(22), 16745–16753. https://doi.org/10.1021/la102461z

Renne, P. R., Cassata, W. S., & Morgan, L. E. (2009). The isotope composition of atmospheric argon $^{40}Ar/^{39}Ar$ geochronology: Time for a change? *Quaternary Geology*, *4*, 288–298. https://doi.org/10.1016/j.quageo.2009.02.015

Roberts, A. P., Almeida, T. P., Church, N. S., Harrison, R. J., Heslop, D., Li, Y., et al. (2017). Resolving the origin of pseudo-single domain magnetic behavior. *Journal of Geophysical Research: Solid Earth*, *122*(12), 9534–9558. https://doi.org/10.1002/2017jb014860

Roberts, A. P., Chang, L., Rowan, C. J., Horng, C. S., & Florindo, F. (2011). Magnetic properties of sedimentary greigite ($Fe_3S_4$): An update. *Reviews of Geophysics*, *49*(1), RG1002. https://doi.org/10.1029/2010RG000336

Roberts, A. P., Cui, Y., & Verosub, K. L. (1995). Wasp-waisted hysteresis loops: Mineral magnetic characteristics and discrimination of components in mixed magnetic systems. *Journal of Geophysical Research*, *100*(B9), 17909–17924. https://doi.org/10.1029/95jb00672

Roberts, A. P., Heslop, D., Zhao, X., & Pike, C. R. (2014). Understanding fine magnetic particle systems through use of first-order reversal curve diagrams. *Reviews of Geophysics*, *52*(4), 557–602. https://doi.org/10.1002/2014rg000462

Roberts, A. P., Pike, C. R., & Verosub, K. L. (2000). First-order reversal curve diagrams: A new tool for characterizing the magnetic properties of natural samples. *Journal of Geophysical Research*, *105*(B12), 28461–28475. https://doi.org/10.1029/2000jb900326

Rowan, C. J., & Roberts, A. P. (2006). Magnetite dissolution, diachronous greigite formation, and secondary magnetizations from pyrite oxidation: Unravelling complex magnetizations in Neogene marine sediments from New Zealand. *Earth and Planetary Science Letters*, *241*(1–2), 119–137. https://doi.org/10.1016/j.epsl.2005.10.017

Rye, R. O. (2005). A review of the stable-isotope geochemistry of sulfate minerals in selected igneous environments and related hydrothermal systems. *Chemical Geology*, *215*(1–4), 5–36. https://doi.org/10.1016/j.chemgeo.2004.06.034

Shaar, R., & Feinberg, J. M. (2013). Rock magnetic properties of dendrites: Insights from MFM imaging and implications for paleomagnetic studies. *Geochemistry, Geophysics, Geosystems*, *14*(2), 407–421. https://doi.org/10.1002/ggge.20053

Smith, G. L., McNeill, L. C., Wang, K., He, J., & Henstock, T. J. (2013). Thermal structure and megathrust seismogenic potential of the Makran subduction zone. *Geophysical Research Letters*, *40*(8), 1528–1533. https://doi.org/10.1002/grl.50374

Steiger, R. H., & Jäger, E. (1977). Subcommission on geochronology: Convention on the use of decay constants in geo- and cosmochemistry. *Earth and Planetary Science Letters*, *36*(3), 359–362. https://doi.org/10.1016/0012-821x(77)90060-7

Surovitskii, L., Makarenko, E., Lukin, M., Smirnov, A. V., Makeev, P., & Alushkin, V. (2022). FORCtool: An online service for rapid analysis of first-order reversal curve (FORC) data. In *AGU fall meeting abstracts* (Vol. 2022, p. GP22A-0275).

Tauxe, L., Mullender, T. A. T., & Pick, T. (1996). Potbellies, wasp-waists, and superparamagnetism in magnetic hysteresis. *Journal of Geophysical Research*, *101*(B1), 571–583. https://doi.org/10.1029/95jb03041

Torsvik, T. H., Van der Voo, R., Preeden, U., Mac Niocaill, C., Steinberger, B., Doubrovine, P. V., et al. (2012). Phanerozoic polar wander, palaeogeography and dynamics. *Earth-Science Reviews*, *114*(3), 325–368. https://doi.org/10.1016/j.earscirev.2012.06.007

Vasconcelos, P. M., Onoe, A. T., Kawashita, K., Soares, A. J., & Teixeira, W. (2002). $^{40}Ar/^{39}Ar$ geochronology at the Instituto de Geociências, USP: Instrumentation, analytical procedures, and calibration. *Annals of the Brazilian Academy of Sciences*, *74*(2), 297–342. https://doi.org/10.1590/s0001-37652002000200008

Vrolijk, P. (1990). On the mechanical role of smectite in subduction zones. *Geology*, *18*(8), 703–707. https://doi.org/10.1130/0091-7613(1990)018<0703:otmros>2.3.co;2

Weibel, R. (1999). Effects of burial on the clay assemblages in the Triassic Skagerrak formation, Denmark. *Clay Minerals*, *34*(4), 619–635. https://doi.org/10.1180/claymin.1999.034.4.08

Yang, T., Petronotis, K. E., Acton, G. D., Zhao, X., Chemale, F., & Vasconcelos, P. (2024). Remagnetization of pre-fan sediments offshore Sumatra: Alteration associated with seismogenic diagenetic strengthening. [Dataset]. *Zenodo*. https://doi.org/10.5281/zenodo.11159341

Yang, T., Zhao, X., Petronotis, K., Dekkers, M. J., & Xu, H. (2019). Anisotropy of magnetic susceptibility (AMS) of sediments from Holes U1480E and U1480H, IODP expedition 362: Sedimentary or artificial origin and implications for paleomagnetic studies. *Geochemistry, Geophysics, Geosystems*, *20*(11), 5192–5215. https://doi.org/10.1029/2019gc008721

Zhang, Q., & Appel, E. (2023). Reversible thermal hysteresis in heating-cooling cycles of magnetic susceptibility: A fine particle effect of magnetite. *Geophysical Research Letters*, *50*(6), e2023GL102932. https://doi.org/10.1029/2023GL102932

Zhang, Q., Appel, E., Basavaiah, N., Hu, S., Zhu, X., & Neumann, U. (2021). Is alteration of magnetite during rock weathering climate-dependent? *Journal of Geophysical Research: Solid Earth*, *126*(10), e2021JB022693. https://doi.org/10.1029/2021JB022693

Zhang, Q., Appel, E., Hu, S., Pennington, R. S., Meyer, J., Neumann, U., et al. (2020). Nano-magnetite aggregates in red soil on low magnetic bedrock, their changes during source-sink transfer, and implications for paleoclimate studies. *Journal of Geophysical Research: Solid Earth*, *125*(10), e2020JB020588. https://doi.org/10.1029/2020JB020588

Zhang, Q., Appel, E., Stanjek, H., Byrne, J. M., Berthold, C., Sorwat, J., et al. (2021). Humidity related magnetite alteration in an experimental setup. *Geophysical Journal International*, *224*(1), 69–85. https://doi.org/10.1093/gji/ggaa394